Isobar Production and Elastic Scattering in p-p Interactions from 6 to 30 GeV/c*

R. M. Edelstein,† R. A. Carrigan, Jr.,‡ N. C. Hien,§ T. J. McMahon,¶ and I. Nadelhaft**
Carnegie-Mellon University, Pittsburgh, Pennsylvania 15213

and

E. W. Anderson, E. J. Bleser,‡ G. B. Collins, T. Fujii,†† J. Menes,‡‡ and F. Turkot
Brookhaven National Laboratory, Upton, New York 11973
(Received 27 September 1971)

Differential cross sections have been measured for nucleon-isobar production and elastic scattering in p-p interactions from 6.2 to 29.7 GeV/c in the laboratory angle range $8 < \theta_{sc} < 265$ mrad. N^*'s at 1236, 1410, 1500, 1690, and 2190 MeV were observed. Computer fits to the mass spectra under varying assumptions of resonance and background shapes show that conclusions on t and s dependence are only slightly affected despite typical variations in absolute normalization of ± 35%. Logarithmic t slopes in the small-$|t|$ range are ~15 (GeV/c)$^{-2}$ for the $N^*(1410)$, ~5 (GeV/c)$^{-2}$ for the N^*'s at 1500, 1690, and 2190 MeV, and ~9 (GeV/c)$^{-2}$ for elastic scattering. Also for the small-$|t|$ data, cross sections for N^*'s at 1410, 1500, 1690, and 2190 MeV and for elastic scattering vary only slightly with P_{inc} consistent with the dominance of Pomeranchuk exchange and with diffraction dissociation. A fit of $N^*(1690)$ total cross sections to the form $\sigma \propto P^{-n}$ gives $n = 0.34 \pm 0.06$, while for elastic scattering $n = 0.20 \pm 0.05$. For the $N^*(1690)$ the effective Regge trajectory has the slope $\alpha_{eff}'(0) = 0.38 \pm 0.17$. When compared with N^* production in π^-, K^-, and $\bar{p}$ beams these data also agree with approximate factorization of the Pomeranchuk trajectory. $N^*(1236)$ cross sections are consistent with other measurements at similar momenta. For $-t > 1$ (GeV/c)^2, elastic scattering cross sections decrease approximately as P_{inc}^{-2}, and they and $N^*(1500)$- and $N^*(1690)$-production cross sections have t slopes consistent with 1.6 (GeV/c)$^{-2}$.

I. INTRODUCTION

This paper reports the results of an experiment on (1) nucleon-isobar (N^*) production in p-p scattering,

$$p + p \to p + N^{*+},$$

and (2) elastic p-p scattering, using the missing-mass technique. The experiment was performed at the Brookhaven AGS. Data were taken at beam momenta of 6.2, 9.9, 15.1, 20.0, and 29.7 GeV/c and over the momentum-transfer-squared range $0.01 < -t < 5.0$ (GeV/c)^2. The N^* peaks[1] which were studied are at the nominal mass values 1236, 1410, 1500, 1690, and 2190 MeV. Some of the results of this experiment[2,3] and of the accompanying study of single-particle spectra[4] have been reported earlier.

In the isobar-production experiment the N^*'s appear in the missing-mass spectra as peaks riding on a smooth background. It is well known that without a precise model for the background and for the resonance shapes (including whether they interfere) the extracted cross sections will have large uncertainties. Therefore, the heart of the N^*-production analysis has been an extensive study of the dependence of the cross sections on the resonance and background shapes. This study shows that the angular distributions and the energy dependence of the cross sections are insensitive to the shapes, despite large variations in absolute normalization.

II. EXPERIMENTAL SYSTEM

A. Missing-Mass Technique

Figure 1 is a schematic drawing of the "missing-mass" system used in this experiment to study the reaction

$$p + p \to p + \mathrm{MM}.$$

A beam proton (1) strikes the target proton (2), and a single proton (3) which recoils from the unidentified particles (4) at a small scattering angle, θ_{sc}, and at high momentum is detected by the recoil spectrometer. The missing mass $M_4 = W$ is given by

$$W^2 = (E_1 + m_p - E_3)^2 - (\vec{P}_1 - \vec{P}_3)^2,$$

where E_1, $\vec{P}_1$, E_3, $\vec{P}_3$ are the energies and momenta of the beam and recoil protons. It is instructive to observe that to lowest order in momentum and scattering angle this formula reduces to

$$W^2 = m_p^2 + 2m_p(|P_1| - |P_3|) - |P_1||P_3|\theta_{sc}^2,$$

so that at small angle the uncertainty in W is given essentially just by the momentum resolution:

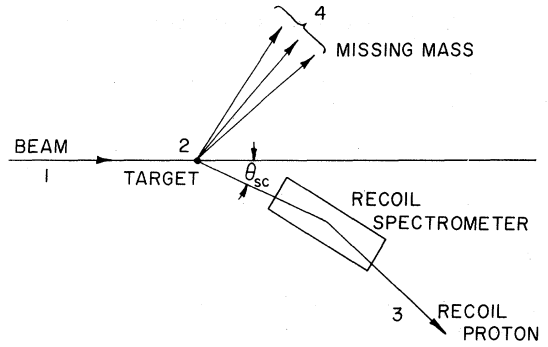

FIG. 1. Schematic representation of the missing-mass experiment $p+p \rightarrow p+X$.

$$\delta W \approx \frac{m_p}{W}[(\delta P_1)^2+(\delta P_3)^2]^{1/2},$$

and is relatively insensitive to the scattering angle θ_{sc}. For a fixed setting and for low missing mass, the momentum resolution was relatively insensitive to the missing mass, so that the mass resolution at W could be calculated simply from the elastic peaks, which were essentially background-free. Typically in this experiment the width of the elastic peak varied from 55 MeV, full width at half maximum (FWHM), at 6.2 GeV/c to 180 MeV at 29.7 GeV/c.

In outline the experimental system consisted of a proton beam, diffraction-scattered from an internal target, and a wire-chamber magnetic spectrometer on line to the Brookhaven PDP-6 computer. Much of the experimental system has been reported previously,[5] so in the ensuing discussion we will stress those aspects which have not been treated before, and in addition repeat the points which are essential to an understanding of the experimental technique.

B. Proton Beam and Hydrogen Target

The beam consisted of protons quasielastically scattered at 1° by an internal Be target at the $F10$ straight section of the AGS. The spill for this experiment was from a special "front porch" of 250 msec in the acceleration cycle during which the beam energy was maintained fixed but with rf bunching retained for post acceleration to full energy. The time of the front porch in the acceleration cycle was varied to obtain our beams at 6.2, 9.9, 15.1, and 20.0 GeV/c whereas for 29.7 GeV/c the standard 500-msec, essentially structureless, flattop was used. Special vacuum tanks were constructed in the target area of the AGS to allow the beam to leave the machine normal to the vacuum window in order to minimize interactions and loss of beam coherence.

The beam transport system is illustrated schematically in Fig. 2. The beam was momentum-analyzed and brought to a first focus at collimator C_5 by dipole magnets D_1 and D_2 and quadrupoles Q_1–Q_4. D_3 swept the beam of low-momentum contamination and quadrupoles Q_5–Q_8 produced a beam at the hydrogen target which was parallel horizontally and slightly convergent vertically. C_2 was a fixed vertical collimator and C_1 was a remotely controlled horizontal collimator used to vary the beam intensity from 10^5 to 10^7 protons/pulse for 5×10^{11} protons/pulse incident on the internal target. The intensities agreed well with expectations based on the solid-angle acceptance of the system and on simple quasielastic scattering from the Be. By varying C_1 we could therefore compensate partially for the wide range of cross sections studied in the experiment. The fluxes into the transport system were quite similar at all momenta since, amusingly enough, for elastic p-nucleon scattering $d\sigma/d\Omega_{lab}$ at 1° is approximately constant. The momentum resolution and horizontal spot size, depended on the settings of C_5 and C_1, respectively. During low-intensity runs at small θ_{sc} typical numbers were

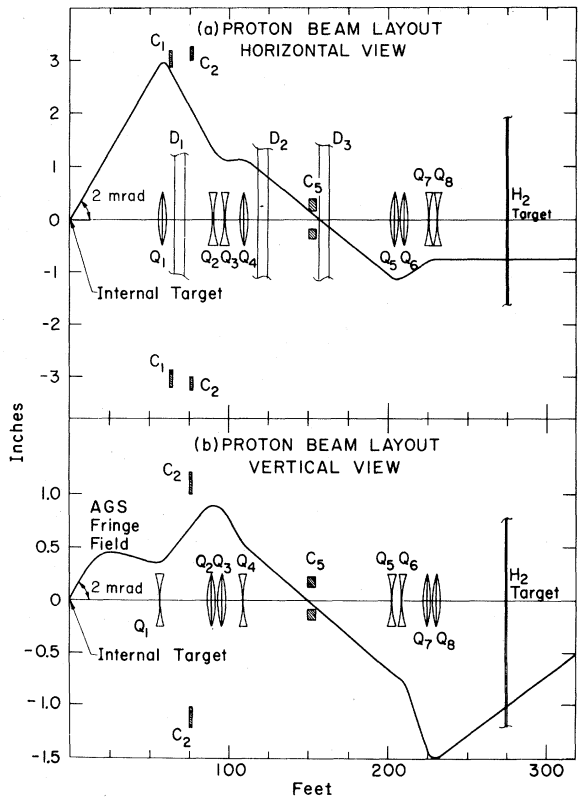

FIG. 2. Layout of the proton-beam transport system: (a) horizontal view, (b) vertical view. D_1, D_2, D_3 are analyzing dipole magnets, Q_1-Q_8 are quadrupole focussing magnets. C_1, C_2, and C_5 are Pb collimators. The solid lines indicate the focussing action of the quadrupole magnets and the AGS fringe field.

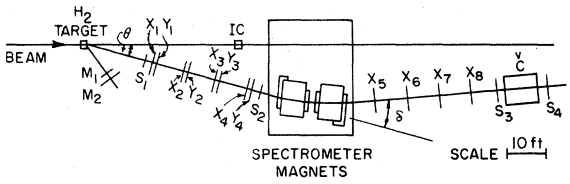

FIG. 3. Layout of the experimental apparatus. Recoil protons scattered by the hydrogen target are analyzed in momentum and scattering angle by the magnetic spectrometer. Wire chambers X_1–X_4 and X_5–X_8 measure the horizontal projections of the track before and after the analyzing magnets. Y_1–Y_4 analyze the vertical projection of the track before the magnets. The chambers are triggered by a coincidence of scintillation counters S_1–S_4 in anticoincidence with Čerenkov counter $\check{C}$. The beam is monitored by the ionization chamber IC and through secondary scatters into monitor M_1M_2.

$\Delta P/P = 0.6\%$, $\Delta V = 2.0$ in., $\Delta H = 0.8$ in., $\Delta\theta_V = 0.8$ mrad, and $\Delta\theta_H = 1.6$ mrad, where $\Delta P/P$ is momentum resolution, ΔV and ΔH are vertical and horizontal spreads at the hydrogen target, and $\Delta\theta_V$ and $\Delta\theta_H$ are vertical and horizontal angular divergences. All values are FWHM. The beam momentum was kept fixed to within $\pm 0.2\%$ for a given set of runs, and small adjustments were made to D_3 at the beginning of each run to maintain the beam on the target center. The error in resetting the momentum was at most $\pm 1.2\%$, and more typically $\pm 0.5\%$, judging from the position of the elastic peak.

The beam was monitored by the ionization chamber IC placed on the beam line downstream from the target, and secondarily by the scintillation telescope M_1M_2 placed at 22° to the beam line (see Fig. 3). These monitors were calibrated in turn by a separate scintillation-counter telescope placed downstream from IC on the beam line, during special low-rate runs. Because of scattering in the target, this telescope counted $(97.5 \pm 1.0)\%$ of the beam.

The liquid-hydrogen target was of a standard Dewar type 8 in. long and 6 in. in diameter with $(0.85 \pm 0.03) \times 10^{24}$ protons/cm^2.

C. Recoil Spectrometer

The layout of the recoil spectrometer is shown in Fig. 3. The scattering angle and momentum were measured by means of wire chambers of the core readout variety placed on either side of the bending magnets D_4 and D_5. Horizontal and vertical projections of θ_{sc} were measured by chambers X_1–X_4 and Y_1–Y_4, respectively, upstream of D_4, and the horizontal projection of the magnetically deflected proton by X_5–X_8. Four chambers were used to measure each straight-line projection. Since only three of four sparks were required to fit a straight line, both high efficiency and clear track identification were achieved in the reconstruction program.

The wire spacing in all chambers was 0.05 in., and they varied in size from 3.2 in.×3.2 in. for X_1 and Y_1 to 8 in.×17.6 in. for X_5–X_8. Equal spacing of 10 ft between neighboring chambers was maintained in each set, and He bags were used throughout the spectrometer to minimize multiple scattering. The apertures of the bending magnets, BNL type 30D72, were 6 in. high×30 in. wide×72 in. long, and their fields were maintained to ±0.1% for a given setting. The mean total bend angle varied from 210 mrad at 6.2 GeV/c to 70 mrad at 29.7 GeV/c. At a given setting the acceptances of the system were $\Delta\theta_{sc} = 14$ mrad, $\Delta\Omega = 10^{-4}$ sr, and $\Delta P/P = 8$–25% depending on the bend angle. The resolutions of the spectrometer were dominated by multiple scattering at 6.2 and 9.9 GeV/c and by spark-location precision at 29.7 GeV/c. They were (FWHM) $\delta\theta_{sc} = 0.8$ (0.2) mrad and $\delta P/P = 0.5\%$ (0.4%) at 6.2 GeV/c (29.7 GeV/c).

The trigger telescope was a coincidence of scintillation counters S_1, S_2, S_3, and S_4 in anti-coincidence with the threshold gas Čerenkov counter $\check{C}$ for pion rejection. S_1–S_4 were sized to require that a coincidence correspond to a track through all the chambers and through $\check{C}$, in order to make a meaningful and direct calculation of system efficiency. The Čerenkov-counter sensitive volume was 12 in. high×40 in. wide×70 in. long. It was filled with Freon 12 (CCl_2F_2) to a maximum operating pressure of 20 psig. Although it was not needed for missing mass $<2m_p$ it was used for the high-mass region and for measurements of the pion spectra. From separate tests it was found to be >99% efficient in rejecting pions, and from the appearance of an elastic peak in the pion spectra, $(2.5 \pm 0.5)\%$ of the protons were counted because of interactions and δ rays. Accidental triggers were typically 4% at small θ_{sc} increasing to as much as 70% at the largest θ_{sc}. These were due primarily to random coincidences between two distinct particles upstream and downstream of the magnets.

Because of the length of the system and the propagation time of electronic signals there was ~1 μsec delay between arrival of a particle and firing of the chambers. Upon triggering the chambers, spark information in the cores was read out into the "data handler" wherein the data were recoded and stored in a buffer memory. A dead time of 1.25 msec was imposed on the trigger for readout and to allow the chamber system to recover. As many as 130 events/pulse were stored. At the end of the spill time the buffer memory was dumped onto magnetic tape and into the computer for on-line analysis during the ~2 sec between machine pulses.

TABLE I. Nominal settings for data taking. θ_{sc} is the mean scattering angle in mrad. $|t_{el}|$ is the mean $|t|$ value in $(\mathrm{GeV}/c)^2$ for elastic scattering at the mean scattering angle.

P_{inc} (GeV/c)	6.2		9.9		15.1		20.0		29.7	
	θ_{sc}	$\lvert t_{el}\rvert$	θ_{sc}	$\lvert t_{el}\rvert$	θ_{sc}	$\lvert t_{el}\rvert$	θ_{sc}	$\lvert t_{el}\rvert$	θ_{sc}	$\lvert t_{el}\rvert$
	15	0.0087	15	0.0220	15	0.051	15	0.090	15	0.198
	35	0.047	25	0.061	25	0.141	25	0.249	25	0.55
	60	0.137	35	0.119	35	0.277	35	0.484	35	1.06
			47	0.214	47	0.495	47	0.90	47	1.88
			60	0.346	60	0.80	60	1.38		
			100	0.93	100	2.10	100	3.60		
			160	2.20	160	5.01				
			260	4.83						

D. Track Reconstruction

The on-line program served the purposes of monitoring the performance of the apparatus and of track reconstruction, both for checking the quality of the data during the run and for later off-line calculation of cross sections.

For each set of chambers X_1–X_4, Y_1–Y_4, and X_5–X_8, a straight line was fitted to the track by least squares if at least three of the four chambers had one and only one spark. The criterion for a good fit was a maximum deviation for any spark of 0.05 in. from the fitted line. Next the momentum was calculated using a square-field approximation for the magnets, and the upstream track was projected through the magnets (using the calculated momentum) to test its line up with the downstream track. Typically the criterion for this test was agreement within ±0.2 in. at chamber X_5. Information such as momentum, polar and azimuthal scattering angles, and transverse position of the track at the target center was then calculated and stored on magnetic tape. The program also sorted the data into several histograms in various of the kinematic quantities, such as recoil momentum, for printout at the end of each run. This printout also included data on the performance of the system such as frequency of misses and multiple sparks for each plane and track reconstruction efficiency. The over-all track-reconstruction efficiency was typically 85%.

The on-line program was fast enough, 15 msec/event, to process all data on line. There were some runs for which the computer was not operative, and in this case the raw-data tapes were processed off line on the PDP-6.

E. Run Plan

The running scheme was to set the apparatus for a fixed mean scattering angle and then take data at each beam momentum, changing the mean bend angle in the dipole magnets to maintain near-maximum field. At each setting, target-empty background runs were taken. Typically the background was <5% of the full count. Over-all, continuous data were taken in five $\langle\theta_{sc}\rangle$ settings from 8 to 67 mrad and large-angle data then sampled at 100, 160, and 260 mrad. Operation of the front porch near the transition energy of the AGS was unstable so only three $\langle\theta_{sc}\rangle$ settings were taken at 6.2 GeV/c.

The nominal settings for P_{inc}, θ_{sc}, and t_{el} are given in Table I. At each setting data were usually taken at two or three settings of the magnetic field in order to cover the whole mass range of interest for the whole angle range. A total of 3×10^7 events were taken in the experiment.

III. DATA ANALYSIS

In this section we discuss the analysis of the data from the output of the on-line program to elastic scattering cross sections and to the final inelastic missing-mass spectra from which isobar cross sections were later evaluated.

A. System Acceptance

It is necessary at this point to discuss in detail the scattering-angle and recoil-momentum (hence missing-mass) acceptance of the system. Figure 4(a) illustrates the definition of "unbiased" acceptance. Rectangle R_3 is the projection of counter S_3 on a plane through its center and transverse to the beam line. Point B is the intersection of the beam line with this plane. Area A corresponds to scattering in the interval $\Delta\theta_{sc}$ about a mean θ_{sc} of a particle of unique momentum. The azimuthal acceptance $\Delta\phi$ was calculated simply from the geometry of the system. A similar diagram pertains at other apertures such as R_2 which corresponds to counter S_2, but with larger $\Delta\phi$ in all cases so that $\Delta\phi$ was defined by S_3 only. The boundaries of A were slightly fuzzy because of the beam divergence, momentum spread, and finite size at the target. If for unique missing-mass and scattering-angle intervals no such areas were terminated by vertical edges of apertures (chambers, counters, or mag-

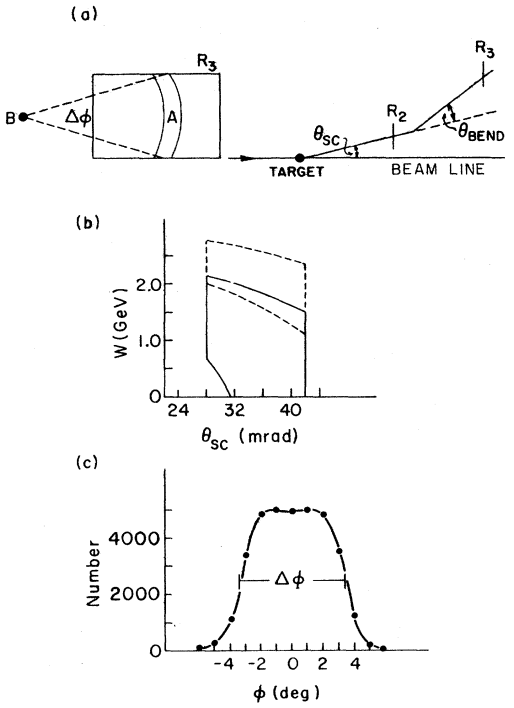

FIG. 4. Acceptance of the spectrometer in missing mass W, scattering angle θ_{sc}, and azimuthal angle ϕ. (a) Projection of vertically defining counter S_3 transverse to the beam. A represents the area into which particles at a unique momentum are scattered for scattering angle $\theta \pm \Delta\theta$ and azimuthal angle range $\Delta\phi$. (b) Typical acceptance in W and θ_{sc} at a fixed physical set up. The solid and dashed lines represent the boundaries of "unbiased" data for two different magnet current settings. (c) Typical ϕ distribution of events for fixed θ_{sc}.

nets) the data were termed "unbiased."

For a given magnet setting the unbiased missing-mass range varies with θ_{sc} as illustrated in Fig. 4(b). The two overlapping areas correspond to a fixed angle setting with two different magnetic fields. In practice, $\Delta\phi$ was evaluated from the data. Figure 4(c) is an example of the distribution of events in ϕ at fixed θ_{sc} and missing mass. The full width at half height agreed within ±3% with calculated values. All data used in the experiment were "unbiased" except at large scattering angle where for small cross sections, the large beam size necessary with high flux precluded defining any such region. However, we estimate that the error introduced there was $\lesssim$10% and the statistical errors were large in any case.

B. Data Reduction

For each setting the data were sorted into two dimensional bins of W and θ_{sc}, with bin sizes usually 30 MeV and 2 mrad, respectively. Differential cross sections $d^2\sigma/dW d\Omega_{lab}$ were calculated and corrected for chamber readout dead time, and for system efficiency, which was defined as

$$\frac{\text{fitted events}}{\text{triggers} - \text{accidental triggers}} .$$

The target-empty background was subtracted next using the same efficiency as was used for corresponding target-full data.

Uncorrected elastic cross sections, $d\sigma/dt$, were evaluated by summing the data for $0.81 < W < 1.07$ GeV. Small differences in absolute normalization between settings were corrected by adjusting for equality of the data in overlapping t bins, or for smooth t dependence where no overlap existed. These differences were due to uncertainties in the system efficiency and beam normalization and were smaller than ±8%. The correction factor was assumed to be 1.00 for the 25-mrad settings and for the widely spaced data at $-t > 1$ (GeV/c)^2. Small corrections were made to the mass scale on the basis of the position of the elastic peaks, at most ±30 MeV, and their widths noted for later use in N^* cross-section evaluation. Systematic errors of ±4% have been assigned to each elastic data point to account for small nonuniformities in the system and for uncertainties in the relative intersetting normalization.

Additional corrections to the elastic scattering data were required for (1) absorption in the target +3.6%, (2) absorption in the spectrometer and counters +(4.0 ± 0.5)%, (3) beam-counting inefficiency −(2.5 ± 1.0)%, (4) plural elastic scattering (an angle-dependent correction), and (5) inelastic tail under the elastic peak (also angle-dependent). Plural scattering in the target, two or more elastic scatters, gives rise to apparent single elastic scattering but with shallower t dependence. For example with a simple exponential dependence, $d\sigma/dt \sim e^{bt}$, $b_{\text{double}} = \frac{1}{2} b_{\text{single}}$. However, the peak is shifted to lower missing mass. This shift is negligible at small angles but increases with $|t|$. Therefore, as noted in Ref. 3, this correction was coupled with the subtraction of the inelastic tail using hand-drawn curves. The correction was small at small $|t|$, e.g., 2–3% at $-t = 0.4$ (GeV/c)^2, but grew to as much as (25 ± 15)% in the region of $-t = 1$ (GeV/c)^2. Corrections (1)–(3) were made to the inelastic data also, and contributions similar to (4) are discussed in Sec. V.

Finally, as discussed in Sec. IV, the elastic data were renormalized to agree with the optical theorem at $t = 0$, and the inelastic data adjusted accordingly.

As a step toward preparing inelastic spectra for computer fitting, the high-mass tail of the elastic peak was subtracted from the region $W > 1.05$ GeV.

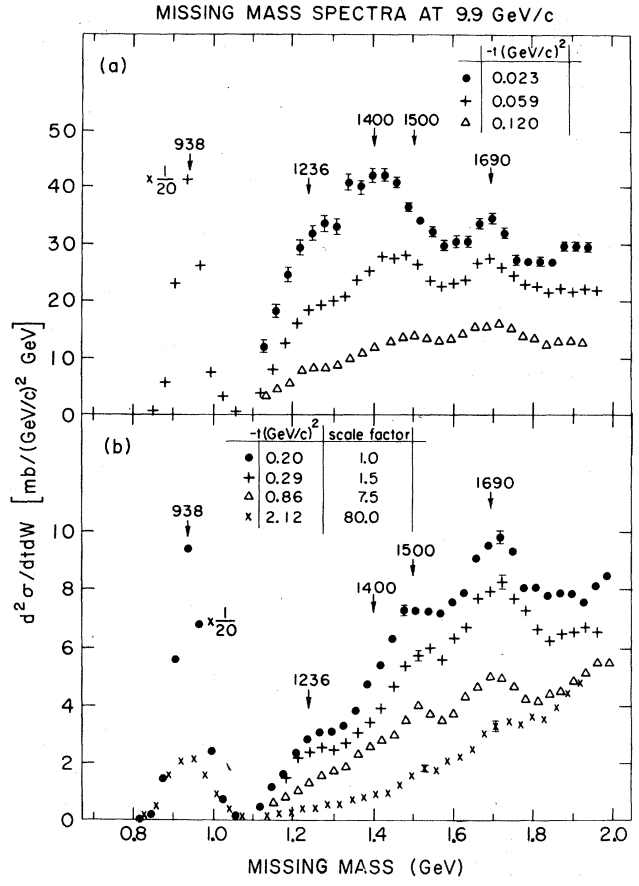

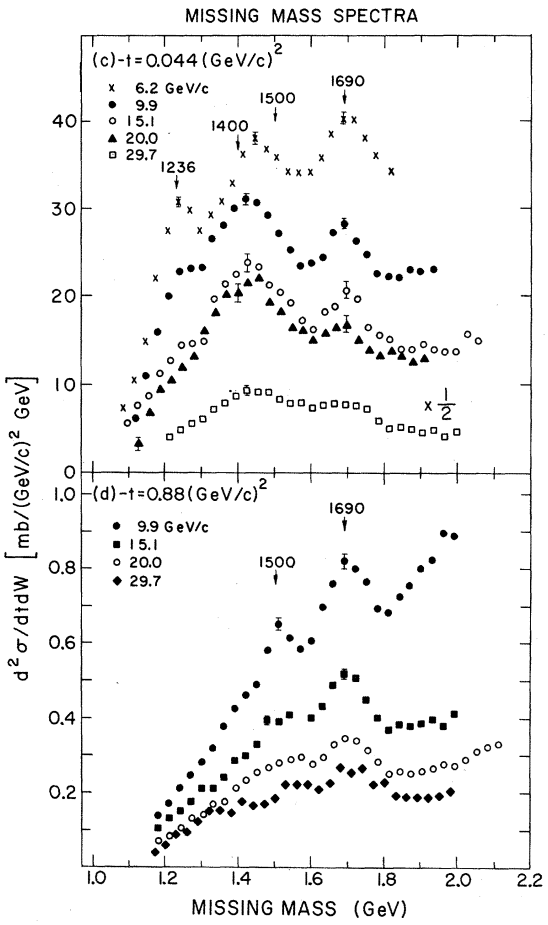

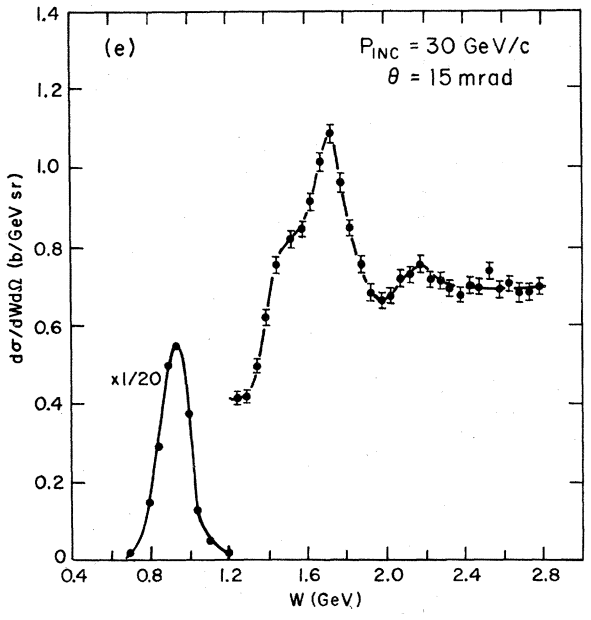

FIG. 5. Sample missing-mass spectra for $p+p \to p+X$. (a) and (b) Spectra for 9.9 GeV/c for several t values from 0.023 to 2.12 (GeV/c)^2. Also included are representative elastic peaks associated with these plots. (c) Spectra at $-t=0.044$ (GeV/c)^2 for data from 6.2 to 29.7 GeV/c. (d) Spectra at $-t=0.88$ (GeV/c)^2 for data from 9.9 to 29.7 GeV/c. (e) High-mass spectrum at 29.7 GeV/c taken from Ref. 2. Note that all these plots are for fixed scattering angle and that the quoted t values are for $W=1500$ MeV. See Refs. 6 and 7 for further discussion.

Since the elastic peaks were not symmetric below the 5% level, it was possible to use only a hand-drawn tail, and therefore the spectra could not be fit reliably where the subtraction was >30%. The cutoff in the N^* fitting was typically at $W_{\min}=1.11$ GeV.

Overlapping data for different analyzing magnet currents at the same P_{inc} and $\langle\theta_{sc}\rangle$ setting were combined to provide unbiased data for $1.1 \lesssim W \lesssim 1.95$ GeV over typically 60% of the 14-mrad bite in θ_{sc}. In order to keep the event count high and to maintain the validity of the fitting procedure,

these data were summed into larger-angle bins, typically one or two per $\langle\theta_{sc}\rangle$ setting. Separate spectra were constructed to include the $N^*(2190)$ and higher masses.

C. Missing-Mass Spectra

Several missing-mass spectra are shown in Fig. 5 to illustrate the qualitative features of the inelastic data.[6] Figures 5(a) and 5(b) show representative spectra at 9.9 GeV/c for $0.020 < -t < 2.20$ (GeV/c)^2. For comparison several elastic peaks are also included. The $N^*(1690)$ is present in all spectra, the $N^*(1500)$ is also clearly present except at low $|t|$, and the $N^*(1236)$ is present only at small $|t|$. The $N^*(1410)$ is also clearly seen at small $|t|$. However, the $N^*(1410)$ and $N^*(1500)$ are not clearly resolved in any of the data. Instead, as $|t|$ increases, one sees a shift of the composite peak from 1410 to 1500 MeV and also a narrowing. Thus, for $-t < 0.1$ (GeV/c)^2 the $N^*(1410)$ dominates and for $-t > 0.3$ (GeV/c)^2 the $N^*(1500)$ dominates.

The energy dependence is illustrated in Figs. 5(c) and (d) for $-t = 0.044$ and 0.88 (GeV/c)^2, respectively.[6,7] At small $|t|$ the Δ is seen to decrease with energy, it is clearly visible at 6.2 and 9.9 GeV/c and not evident at 20.0 and 29.7 GeV/c. The $N^*(1690)$ is seen at all energies and at both low and high $|t|$, and the $N^*(1410)$ is seen at small $|t|$ for $P_{inc} \geq 10$ GeV/c. As will be shown later quantitatively, the production cross sections for $N^*(1410)$, $N^*(1500)$, and $N^*(1690)$ are at most slowly varying functions of momentum for $P_{inc} \geq 10$ GeV/c. (Note that increasing resolution smearing causes peaks to appear less prominent as P_{inc} increases.) A remarkable feature of the data at small $|t|$ and for missing mass <1.5 GeV is the energy independence of *shape* and *normalization* for $P_{inc} \gtrsim 15$ GeV/c. In addition, at 6.2 GeV/c the "1410 MeV" peak is less prominent vis-à-vis the $N^*(1690)$ than it is at higher P_{inc}. These features, in addition to the approximate constancy of the N^* cross sections, are suggestive of a diffractive-production mechanism for the total signal at small mass as will be discussed further in Sec. VI. At $-t = 0.88$ (GeV/c)^2 there is also a tendency toward energy independence, although it appears that for high $|t|$ this saturation occurs at higher energy than for low $|t|$.

A high-mass spectrum which demonstrates $N^*(2190)$ production at 29.7 GeV/c is shown in Fig. 5(e). This peak was not evident in the data for $P_{inc} \leq 15.1$ GeV/c. There is no convincing evidence for N^* production in the 1900-MeV mass region or at masses higher than 2190 MeV.

IV. ELASTIC SCATTERING

The elastic differential cross sections at 15.1, 20.0, and 29.7 GeV/c were fit to the form Ae^{bt+ct^2} for $-t \leq 0.8$ (GeV/c)^2. The data for 6.2 and 9.9 GeV/c were fit to the simpler form Ae^{bt} because of the limited t ranges for which data were taken. All data were then renormalized to agree with the optical theorem at $t = 0$ using total cross-section data[8] corrected for the real part of the forward scattering amplitude.[8,9] The factors by which the data have been scaled are 0.93, 1.06, 1.14, 1.09, and 1.17 at 6.2, 9.9, 15.1, 20.0, and 29.7 GeV/c, respectively.[10,11] The combined statistical errors in these numbers from the total cross-section measurements and from the fits to the elastic scattering data are small (<5% in all cases) compared with the estimated systematic error in normalization of ±15% due principally to the uncertainties in beam intensity, system geometrical acceptance, and system efficiency. Thus, considering the over-all systematic error, the renormalization factors are consistent with unity.

Final cross sections are given in Table II (a) and plotted in Fig. 6. For the range $-t < 1.1$ (GeV/c)^2 shown in Fig. 6(a) the data show the slight energy dependence previously observed in other work[12] and the near absence of the quadratic term. In Table II (b) we show the results of these fits from which total elastic cross sections have been obtained using the formula

$$\sigma_{el} = \frac{A}{b}\left(1 + \frac{2c}{b^2}\right).$$

The total elastic cross sections decrease slightly with energy. The ratio σ_{el}/σ_T is 0.21 at 29.7 GeV/c. A fit to the form $\sigma_{el} \propto P^{-n}$ yields

$$n = 0.20 \pm 0.05,$$

again similar to earlier results.

As has been discussed in Refs. 2 and 3 our data in the high-t region indicate a break in the cross sections at $-t \sim 1.2$ (GeV/c)^2 such that the slope in the large-$|t|$ region is 1.6 (GeV/c)$^{-2}$. Furthermore, contrary to the behavior at small $|t|$ these data show a marked energy dependence, decreasing appropriately as P_{inc}^{-2}. This behavior has been studied in detail by Allaby *et al.*,[13] and our data, where comparable, are in excellent agreement with theirs.

V. EVALUATION OF ISOBAR-PRODUCTION CROSS SECTIONS

A. Outline of the Procedure

At each beam momentum missing-mass spectra were compiled for each of several small intervals in scattering angle. A least-squares fitting technique was used to extract the areas of the bumps for each of these spectra using an expression which was the sum of resonance terms plus smooth background.

TABLE II. Elastic scattering cross sections. All t values are in $(\mathrm{GeV}/c)^2$, and differential cross sections are in mb/$(\mathrm{GeV}/c)^2$. Cross sections have been renormalized to agree with total cross sections through the optical theorem as discussed in the text and Ref. 10. The factors are 1.06, 1.14, 1.09, and 1.17 at 9.9, 15.1, 20.0, and 29.7 GeV/c, respectively.

(a) Differential elastic scattering cross sections

9.9 GeV/c		15.1 GeV/c		20.0 GeV/c		29.7 GeV/c	
$-t$	$d\sigma/dt$	$-t$	$d\sigma/dt$	$-t$	$d\sigma/dt$	$-t$	$d\sigma/dt$
0	90.5	0	84.2	0	80.7	0	...[a]
0.016	77.1±3.1	0.027	71.4±3.0	0.032	62.6±2.5	0.079	37.4±1.9
0.022	71.9±2.9	0.038	62.5±2.6	0.048	54.1±2.2	0.097	30.6±1.6
0.028	68.6±2.7	0.051	52.2±2.2	0.067	43.4±1.7	0.116	25.0±1.2
0.035	68.8±2.8	0.066	47.1±2.0	0.090	34.5±1.4	0.137	19.5±1.0
0.043	65.1±2.6	0.082	43.5±1.8	0.115	27.8±1.1	0.160	15.3±0.8
0.052	58.7±2.3	0.100	36.7±1.5	0.144	21.6±0.9	0.184	12.2±0.6
0.061	54.0±2.2	0.120	30.3±1.2	0.176	16.5±0.7	0.211	9.5±0.4
0.071	49.1±2.0	0.141	24.5±1.0	0.211	12.2±0.5	0.238	7.8±0.4
0.082	45.7±1.8	0.165	20.0±0.8	0.249	8.61±0.34	0.268	6.1±0.3
0.093	39.2±1.6	0.190	16.4±0.7	0.290	6.09±0.24	0.299	4.8±0.3
0.105	35.2±1.4	0.217	13.0±0.6	0.334	4.18±0.17	0.333	3.44±0.18
0.118	31.5±1.3	0.275	6.70±0.28	0.381	2.83±0.11	0.367	2.66±0.13
0.131	28.1±1.2	0.307	5.48±0.23	0.433	1.78±0.07	0.382	2.28±0.12
0.146	24.1±1.0	0.341	4.60±0.19	0.486	1.10±0.05	0.458	1.18±0.06
0.161	21.3±0.9	0.376	3.91±0.16	0.542	0.658±0.028	0.541	0.57±0.03
0.215	13.9±0.6	0.452	1.87±0.08	0.601	0.453±0.020	0.630	0.257±0.013
0.234	12.3±0.5	0.492	1.35±0.06	0.664	0.258±0.013	0.726	0.113±0.005
0.253	10.4±0.5	0.534	0.98±0.04	0.732	0.145±0.006	0.834	0.0401±0.0020
0.273	8.1±0.3	0.578	0.69±0.03	0.800	0.085±0.004	0.943	0.0138±0.0014
0.316	5.3±0.2	0.623	0.449±0.019	0.871	0.0436±0.0017	1.060	$(5.5\pm0.9)\times10^{-3}$
0.339	4.60±0.19	0.683	0.265±0.013	0.945	0.0252±0.0010	1.181	$(3.2\pm0.6)\times10^{-3}$
0.362	3.94±0.16	0.732	0.177±0.010	1.022	0.0145±0.0010	1.32	$(1.66\pm0.29)\times10^{-3}$
0.385	3.15±0.13	0.783	0.121±0.007	1.102	$(6.87\pm0.73)\times10^{-3}$	1.45	$(2.23\pm0.33)\times10^{-3}$
0.905	0.083±0.006	0.834	0.086±0.006	1.203	$(6.41\pm0.46)\times10^{-3}$	1.59	$(1.68\pm0.29)\times10^{-3}$
0.941	0.075±0.005	0.888	0.059±0.004	1.287	$(4.72\pm0.39)\times10^{-3}$	1.74	$(1.14\pm0.12)\times10^{-3}$
0.977	0.062±0.004	2.055	$(2.54\pm0.15)\times10^{-3}$	1.375	$(4.07\pm0.33)\times10^{-3}$	1.89	$(0.84\pm0.12)\times10^{-3}$
1.013	0.049±0.004	2.134	$(2.21\pm0.13)\times10^{-3}$	1.464	$(3.60\pm0.31)\times10^{-3}$	2.05	$(0.82\pm0.11)\times10^{-3}$
1.051	0.0407±0.0028	2.214	$(2.08\pm0.13)\times10^{-3}$	1.557	$(3.41\pm0.30)\times10^{-3}$	2.21	$(0.59\pm0.09)\times10^{-3}$
2.250	$(3.55\pm0.32)\times10^{-3}$	2.294	$(1.75\pm0.11)\times10^{-3}$	3.580	$(8.3\pm2.5)\times10^{-5}$	2.78	$(0.36\pm0.16)\times10^{-3}$
2.352	$(2.93\pm0.27)\times10^{-3}$	2.376	$(1.53\pm0.11)\times10^{-3}$	3.847	$(6.3\pm1.9)\times10^{-5}$		
5.078	$(0.191\pm0.019)\times10^{-3}$	4.708	$(4.35\pm1.03)\times10^{-5}$				
		4.914	$(2.96\pm0.90)\times10^{-5}$				

(b) Fitted parameters for $d\sigma/dt = A\exp(bt+ct^2)$ and $\sigma_{el} \propto P^{-n}$

P_{inc} (GeV/c)	9.9	15.1	20.0	29.7
A [mb/$(\mathrm{GeV}/c)^2$]	90.5	84.2	80.7	71.0[a]
b $(\mathrm{GeV}/c)^{-2}$	8.95±0.06	8.81±0.25	9.17±0.11	9.34±0.28
c $(\mathrm{GeV}/c)^{-4}$	...	0.60±0.33	0.74±0.14	0.69±0.34
σ_{el} (mb)	10.2 ±0.5	9.7 ±0.5	9.0 ±0.5	8.2 ±0.6[b]
		$n = 0.20\pm0.05$		

[a] As discussed in Ref. 10 the renormalization constant for the 29.7-GeV/c data is intermediate between two extreme values. Therefore the intercept at $t=0$ is not the optical point value, 78.3 mb/$(\mathrm{GeV}/c)^2$.

[b] This error accounts for the full range of possible values as discussed in Ref. 10.

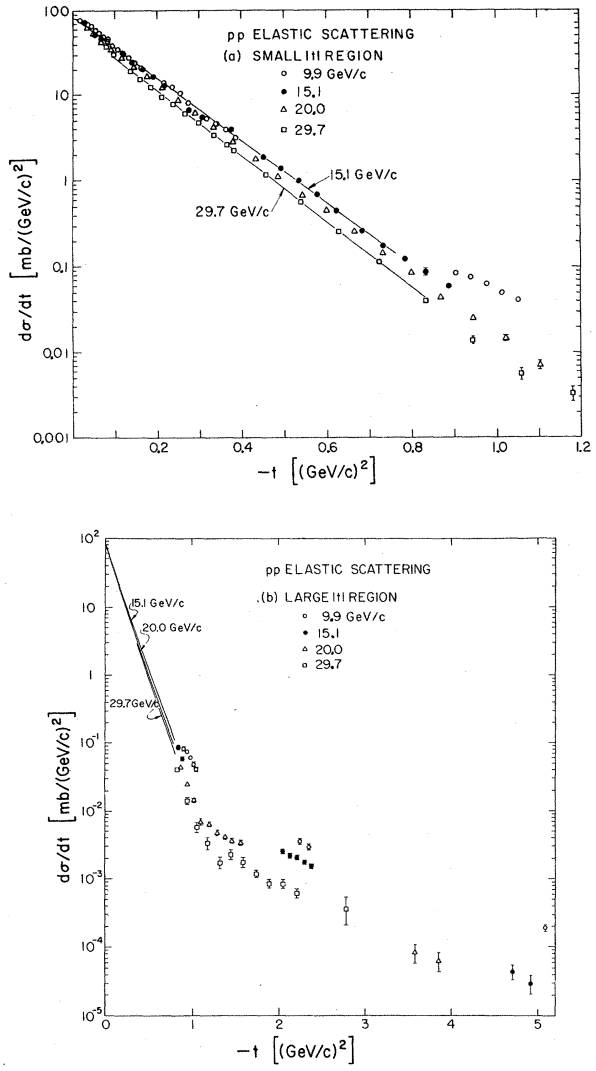

FIG. 6. Elastic p-p scattering data. Data have been renormalized to total cross-section data through the optical theorem. (a) $-t<1.2$ $(\mathrm{GeV}/c)^2$. (b) $-t<5$ $(\mathrm{GeV}/c)^2$.

Of the peaks seen in the data only the resonance at mass 1236 MeV is well explained. The 1410-MeV bump is still not clearly understood, and from phase-shift analyses there are several possible isobars contributing to the higher-mass peaks. For simplicity we make the following assumptions: There is one resonance with fixed width and central mass for each bump seen, and there is no interference between resonances or between a resonance and the nonresonant background. Although interference could alter the cross sections significantly, its inclusion would make the fitting procedure excessively complicated.

The fitting was further complicated by ignorance of (1) the precise shape of the background, (2) the resonance shapes, particularly in the "tail region" well away from the central mass, and (3) the central masses and natural widths of the resonances *(a priori)*. Therefore, before fitting for cross sections, the masses and widths of each resonance were extracted from those spectra where it was prominent and for which there were good statistics. Differential cross sections and their t dependences, and total production cross sections and their energy dependences were then derived from the mass spectra. For all the fitting, the extracting of resonance parameters, and the finding of differential cross sections and the quantities derived from them, extensive studies were made of the dependence on (1) the background shape, (2) the resonance shape, and (3) the resonance parameters, in order to assign uncertainties from all possible sources.

The quoted cross sections for the N^*'s at 1236, 1410, 1500, and 1690 MeV are from the computer fits. The cross sections for $N^*(2190)$ production given in Ref. 2 are included for completeness.

B. The Form Used in Least-Squares Fitting

The following functional form was fit to $d^2\sigma/dWd\Omega_{\mathrm{lab}}$ for each spectrum:

$$F(W)=B(W)+\sum_j A_j R_j(W;W_{0j},\Gamma_j,N). \tag{1}$$

The first term represents the smooth background, and the second term is the sum of the resonance terms.

The background function was

$$B(W)=B_0(W-W_{\mathrm{th}})^{1/2}+\sum_{k=1}^{K} B_k(W-W_{\mathrm{th}})^k, \tag{2}$$

where $W_{\mathrm{th}}=1.073$ GeV is the threshold for the inelastic spectrum.[14] Thus, the background form gives the correct two-body phase-space behavior near threshold where the first term dominates, but it has no further physical significance. Since these are missing-mass spectra, with several channels contributing, it is not possible to represent the background with a single phase-space curve.

Each resonance was represented by a simple Breit-Wigner form taken to the Nth power:

$$R_j(W;W_{0j},\Gamma_j,N)=\mathfrak{N}[(W-W_{0j})^2+(\tfrac{1}{2}\Gamma_j')^2]^{-N}, \tag{3}$$

where W_{0j} is the central mass of the peak, Γ_j is

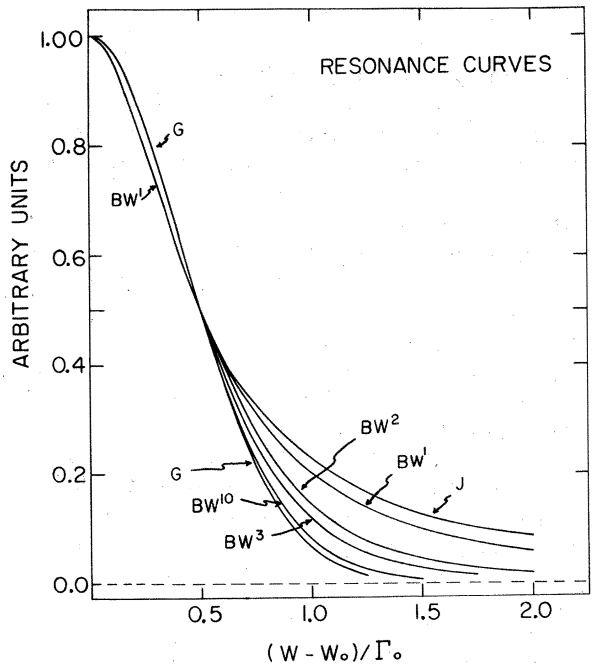

FIG. 7. Resonance curves used for extracting N^* cross sections from the spectra. J – Jackson form, G – Gaussian. BW^1, BW^2, BW^3, and BW^{10} are Lorentzian expressions raised to the first, second, third, and tenth power as discussed in the text. All curves have been adjusted for the same width at half height.

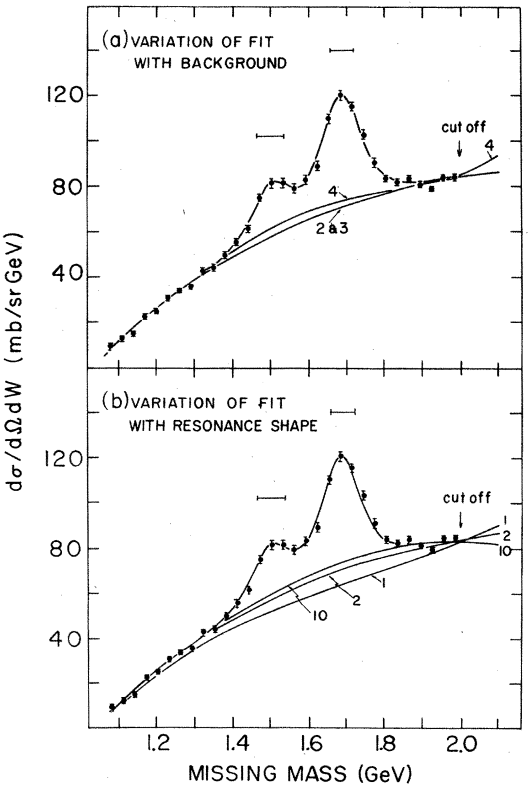

FIG. 8. Fits to sample data at 15.1 GeV/c and 42 $< \theta_{sc} <$ 50 mrad with varying resonance and background shapes. In all cases the fits are acceptable so the curves through the data are almost identical. (a) Background variation. Curves labeled 2, 3, and 4 are the fitted backgrounds for background polynomials of orders 2, 3, and 4. (b) Resonance-shape variation. Background curves are for fits with resonance-shape parameter values $N = 1$, 2, and 10. The horizontal bars represent the resolution at the $N^*(1500)$ and $N^*(1690)$ peaks, computed from the elastic peaks.

its width (FWHM), N is an integer, Γ_j' is an adjusted width parameter which gives Γ_j = FWHM (for $N = 1$, $\Gamma_j' = \Gamma_j$), and $\mathfrak{N}$ is a normalization constant which gives $\int_{-\infty}^{\infty} R_j dW = 1$. Therefore, the differential cross section for the jth bump, $d\sigma/d\Omega_{\text{lab}}$, is given directly by the fitted value A_j. This form was used so that one could vary the contribution to the area from the tail of the resonance simply by changing N. Figure 7 shows the functional form for fixed W_0 and Γ and for several values of N. Also shown are the Gaussian and Jackson s-wave forms,[15] also with the same width. Note that these forms are quite similar to Eq. (3) with $N = 10$ and 1, respectively, except at large values of $|W - W_0|$ where the contribution to the area is small in any case.

As is apparent there is no dependence on the resonance decay momentum in this form to take account of intrinsic angular momentum and two-body phase space. Not only did this facilitate programming, but it was considered acceptable for several reasons: (1) The shape of the tail region is uncertain and there is considerable background in all cases. (2) The precise form of an inelastic resonance with several decay channels is even more uncertain than for an elastic one (only the Δ is elastic). (3) We still do not know for sure exactly what the mass-1410-MeV peak is.

The range of masses fit to this form was typically $1110 < W < 1950$ MeV. At the low end a compromise was struck between staying well below the Δ peak and well above the threshold where there were large uncertainties connected with the subtraction of the elastic peak. The background at high mass was established adequately with the cutoff at $\approx$1950 MeV well above the 1690 MeV peak. The inclusion of unbiased data at higher masses, while desirable, would have limited severely the amount of usable data.

For each spectrum and for each variation of the other parameters, fits were made with $K = 2, 3, 4$ [see Eq. (2)]. Higher values of K gave too much structure to the background. In this way the sensi-

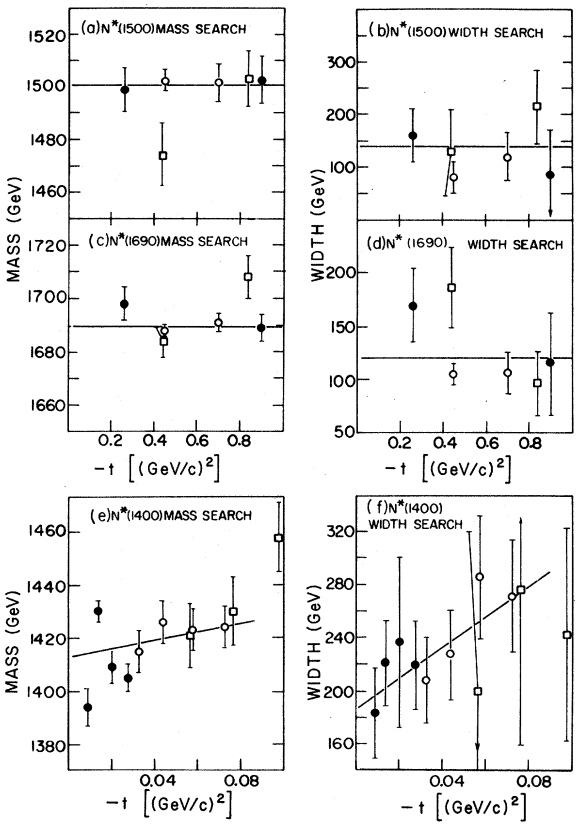

FIG. 9. Position and width searches for the N^*'s. ●, ○, □ represent data for 9.9, 15.1, 20.0 GeV/c, respectively. (a) and (b) Position and width search for the $N^*(1500)$. (c) and (d) Position and width search for the $N^*(1690)$. The horizontal lines represent the average values in each case. (e) and (f) Position and width search for the $N^*(1410)$. The solid lines are linear fits to the data.

tivity to background shape was studied. Each fitted parameter was then averaged over the three values, and the average statistical error was enlarged by half the full spread. This contribution to the error was typically 10% and in no case more than 20%. χ^2 was generally good in all cases. An example of the variation in background shape with K is given in Fig. 8(a). The spectrum is for $P_{\text{inc}} = 15$ GeV/c and the scattering-angle range

$$42 < \theta_{\text{lab}} < 50 \text{ mrad}.$$

The values of N [see Eq. (3)] were the same for all resonances in each of the fits made. Figure 8(b) shows the variation in fit with N for the same data as above. Again the quality of fit is good in all cases.

C. Central Masses and Natural Widths of the Resonances

A modified least-squares fitting routine was used to search the positions and widths of the 1410-, 1500-, and 1690-MeV peaks. The pertinent resonance terms in Eq. (1) were replaced by first-order expansions about starting values for the parameters W_{0j} and Γ_j, and the increments along with the A_j and the background were fit by iteration. By this means $F(W)$ was kept linear in adjustable parameters so as to keep track of all errors readily. The relation between the width parameter used, or found in fitting, and the natural width is taken as

$$\Gamma_j^2 = \Gamma_{0j}^2 + r_j^2, \tag{4}$$

where

$$r_j \approx \frac{M_p}{W_{0j}} \delta W|_{M_p}. \tag{5}$$

Γ_{0j} is the intrinsic width of the resonance, r_j is the system resolution at W_{0j}, and $\delta W|_{M_p}$ is the experimentally observed resolution width of the elastic peak. This simple relation is a good one for the central region of a peak though the tail is exaggerated somewhat. Searches were made at several values of N, and for beam momenta of 9.9, 15.1, and 20.0 GeV/c. At all times the Δ was kept fixed at $W_0 = 1236$ MeV and $\Gamma = 125$ MeV.

Not all the peaks were studied simultaneously. First the parameters for the $N^*(1500)$ and $N^*(1690)$ were searched in the region $0.3 < -t < 1.0$ (GeV/c)^2 in data for which there is no evidence of the Δ and $N^*(1410)$. The P_{inc} and t dependence of these parameters for $N = 2$ is displayed in Figs. 9(a)–9(d). Within the precision of the data these parameters are constant. Therefore average values were found for each value of N.

The 1410-MeV peak was studied in the data with

TABLE III. Resonance masses and widths vs shape parameter N.

Resonance	N [a]	Mass (MeV)	Width (MeV)
$N^*(1410)$	1	1409 ±8	203±30
	2	1413 ±8	186±24
	3	1413 ±8	184±21
	10	1410 ±9	176±19
$N^*(1500)$	1	1499.4±2.7	146±35
	2	1500.5±2.9	115±19
	3	1502.3±2.7	136±23
	10	1504.6±3.2	158±10
$N^*(1690)$	1	1690.2±4.1	149±12
	2	1689.5±2.6	120±11
	3	1691.0±4.4	123±11
	10	1691.2±4.0	129±10

[a] See Sec. V B for definition of N.

TABLE IV. Resonance masses and widths.[a]

Data on mass spectra											
Δ		$N^*(1410)$		$N^*(1500)$		$N^*(1690)$		$N^*(2190)$			
Mass	Width	Mass	Width	Mass	Width	Mass	Width	Mass	Width	Type of experiment	Reference
1236[b]	125[b]	1411 ± 10	188 ± 38	1501 ± 5.6	140 ± 43	1690.3 ± 4.5	133 ± 26	2190[b]	...[b]	$pp \to pN^*$, Missing mass	This experiment
1217 ± 8	92 ± 12	1412 ± 13	200 ± 15	1503 ± 6	105 ± 9	1691 ± 4	119 ± 9	2180 ± 25	265 ± 70	$\pi p \to \pi N^*$, Missing mass	c
1226 ± 5	115 ± 10	...	...	1508 ± 5	80 ± 20	1705 ± 15	85 ± 25	...	...	$ep \to eN^*$, Missing mass	d
1240 ± 6	102 ± 4	1400 ± 10 1410 ± 15	200 ± 20 125 ± 20	1508 ± 2	92 ± 3	1683 ± 3	110 ± 4	...	...	$pp \to pN^*$, Missing mass	e
1231.5 ± 0.6	113 ± 3									$\pi^{\pm}p$ formation exp.	f
...		Mass 1423 ± 27 to 1510 ± 10		Width 58 ± 8 to 124 ± 5		1690 ± 10 to 1732 ± 7	64 ± 20 to 130 ± 30	...	...	$N^* \to \mathfrak{N}\pi\pi$, Production experiments in bubble chamber	g

Phase-shift data[h, i]			
Name	J^P	Mass	Width	Contribute to
$P_{11}(1470)$	$\frac{1}{2}^+$	1470 ± 35	300 ± 100	$N^*(1410)$
$D_{13}(1520)$	$\frac{3}{2}^-$	1520 ± 20	120 ± 25	$N^*(1500)$
$S_{11}(1535)$	$\frac{1}{2}^-$	1535 ± 50	118 ± 50	
$D_{15}(1670)$	$\frac{5}{2}^-$	1672 ± 15	142 ± 35	$N^*(1690)$
$F_{15}(1688)$	$\frac{5}{2}^+$	1688 ± 10	127 ± 40	
$S_{11}(1700)$	$\frac{1}{2}^-$	1706 ± 50	256 ± 150	
$S_{31}(1650)$	$\frac{1}{2}^-$	1650 ± 40	150 ± 60	
$D_{33}(1670)$	$\frac{3}{2}^-$	1674 ± 20	240 ± 60	
$G_{17}(2190)$	$\frac{7}{2}^-$	2180 ± 50	300	$N^*(2190)$

[a] All masses and widths are in MeV.
[b] Position and width not searched in this experiment.
[c] See Ref. 17.
[d] See Ref. 18.
[e] The values for the Δ, $N^*(1500)$, and $N^*(1690)$ are from Ref. 19. The two sets of values for the $N^*(1410)$ are from Refs. 20 and 21, respectively.
[f] See Ref. 22.
[g] See Ref. 23. Quoted values integrated over t, hence one bump in the 1400–1500 MeV mass region.
[h] Only well established resonances which could contribute to the bumps in the present experiment are included.
[i] See Ref. 24. Errors have been expanded to include variations among experiments.

TABLE V. Sets of widths used in fitting. All values are in MeV.

Δ	$N^*(1410)$	$N^*(1500)$	$N^*(1690)$
125	210	100	100
	210	125	100
	210	150	100
	210	175	100
	210	125	75
	210	125	125
	210	125	150
	180	125	100
	240	125	100

$-t<0.1$ (GeV/c)^2 with fixed parameters for the Δ and $N^*(1690)$. In these data the 1410- and 1500-MeV peaks are unresolved although by comparison with $N^*(1500)$ data at higher $|t|$ the $N^*(1410)$ dominates. Therefore one resonance term was assumed in the parameter search.[16] Figures 9(e) and 9(f) show the dependence on P_{inc} and t of this bump for $N=2$. The

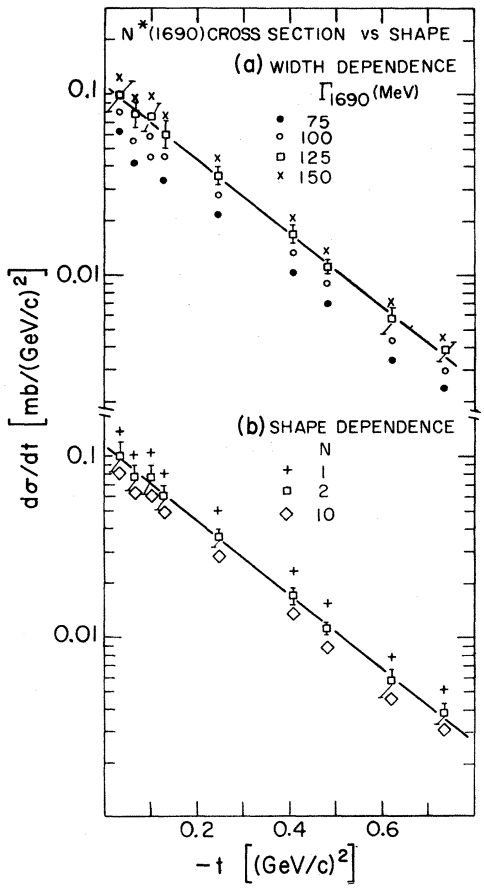

FIG. 10. Variation of differential cross sections with (a) resonance width and (b) resonance shape. Note that although normalization of the data changes markedly with these parameters the changes in logarithmic slope are slight.

distributions can be characterized by a linear dependence on t and no P_{inc} dependence. The assigned values of the $N^*(1410)$ parameters are the intercepts of these curves at $t=0$, where the $N^*(1500)$ contamination is smallest. Extrapolating from later cross-section analysis we find that the $N^*(1500)$ is ≤10% of the $N^*(1410)$ at $t=0$.

The masses and widths for the peaks at 1410, 1500, and 1690 MeV are listed in Table III for each value of N. Note that with a large background the error in the width is expected to be large since as the width is varied the background can adjust to the change. The uncertainty in the width, in turn, gives rise to substantial errors in the cross sections although, as will be shown, not in the P_{inc} and t dependence.

The final average values of the parameters are listed in Table IV along with the parameters and the values obtained (a) in other missing-mass experiments with counter techniques,[17–22] (b) from some representative bubble-chamber experiments,[23] and (c) from phase-shift analysis of low-energy πp scattering.[24] We defer further discussion of these parameters to Sec. VI, except to note here the excellent agreement among the missing-mass experiments on pp, $\pi^- p$, and ep scattering [the $N^*(1410)$ is not observed in ep scattering].

D. Differential Cross Sections

The fitting routine was used to obtain differential production cross sections for the Δ at 6.2, 9.9, and 15.1 GeV/c and the 1410-, 1500-, and 1690-MeV N^*'s at 9.9, 15.1, 20.0, and 29.7 GeV/c. The central masses used are the ones given in Table IV. A complete set of fits was made for each of nine sets of assumed intrinsic widths and for each of four values of $N(1, 2, 3, 10)$, in order to study the dependence of the cross sections on the resonance shapes. It was not economically feasible to vary all the widths independently of each other so a set of central values was chosen, and then each resonance width was varied about its central value one at a time. The sets of widths used are listed in Table V.

Figure 10(a) shows the differential cross sections for $N^*(1690)$ production at 15.1 GeV/c for $\Gamma_{1690}=75$, 100, 125, and 150 MeV, respectively, and with the other parameters held fixed. Figure 10(b) shows the variation of the same data with N for $\Gamma_{1690}=125$ MeV. Several features of the fits are noteworthy: (1) As mentioned before the absolute cross sections depend markedly on the assumed width. (2) The cross-section dependence on the tail contribution is also quite significant at least between $N=1$ and $N=2$. (3) Although not shown in the figure the dependence of one resonance on the width of another is, as is expected, much less strong. (4) There

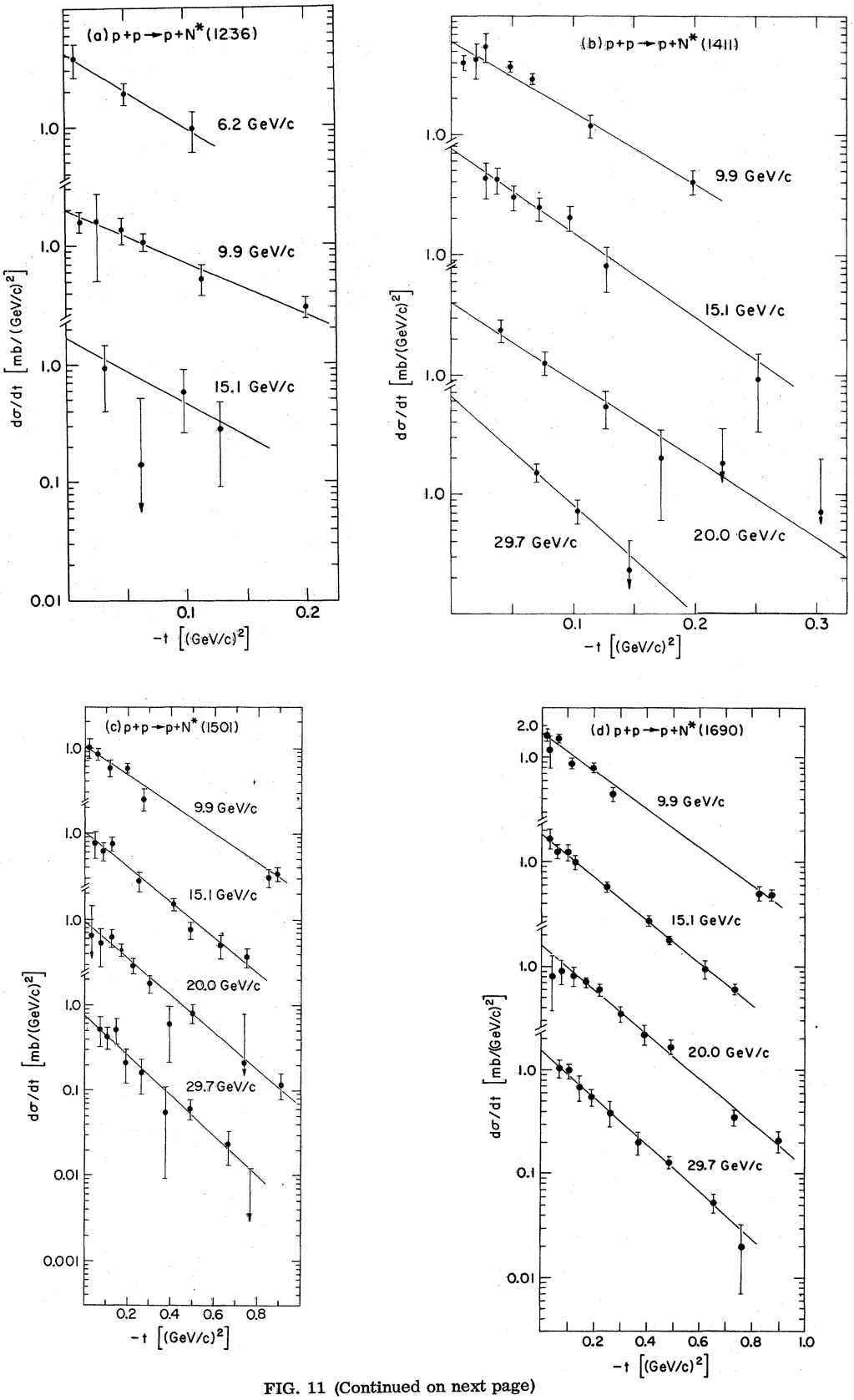

FIG. 11 (Continued on next page)

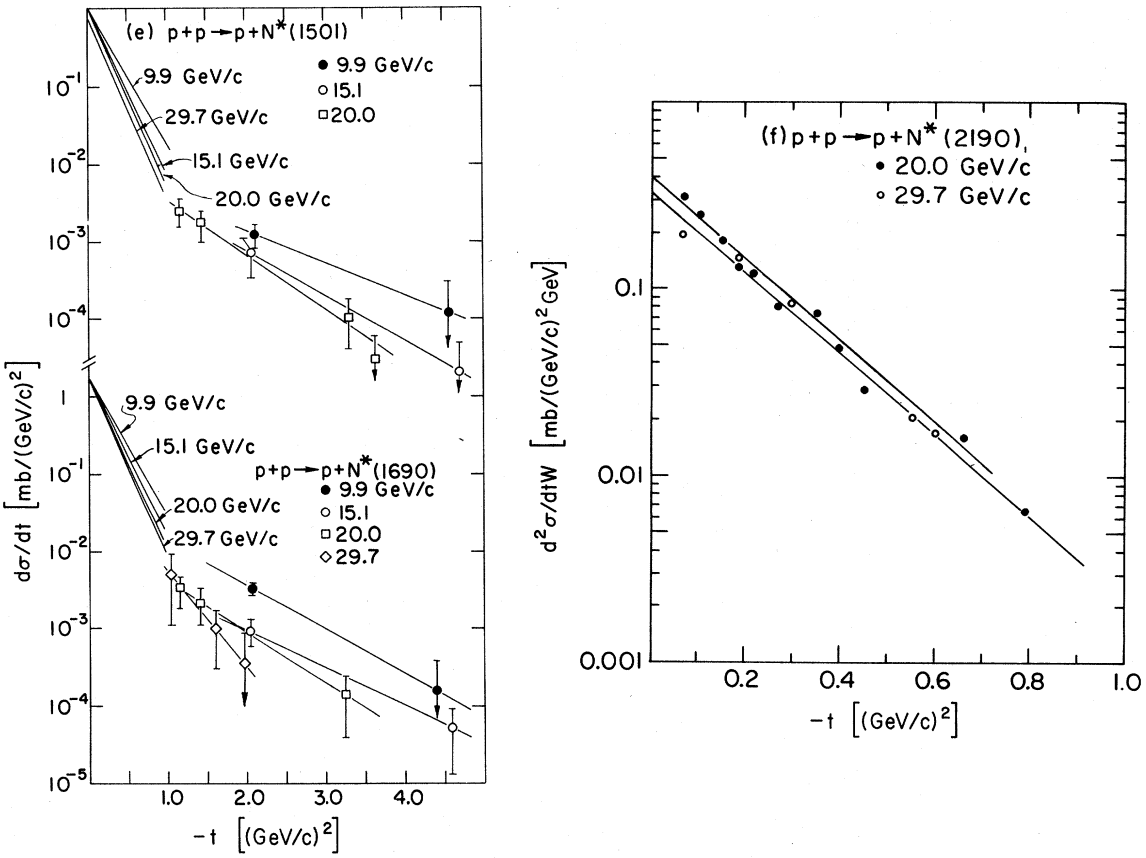

FIG. 11. Differential cross sections for N^* production: (a) $N^*(1236)$, (b) $N^*(1410)$, (c) $N^*(1500)$, (d) $N^*(1690)$. The data for the $N^*(1410)$, $N^*(1500)$, and $N^*(1690)$ are for 9.9, 15.1, 20.0, and 29.7 GeV/c; the data for the $N^*(1236)$ are for 6.2, 9.9, 15.1 GeV/c. All data in (a)–(d) are for $-t<1.0$ (GeV/c)^2. (e) $N^*(1500)$ and $N^*(1690)$ for $-t<5$ (GeV/c)^2. (f) $N^*(2190)$ at 20.0 and 29.7 GeV/c for $-t<0.8$ (GeV/c)^2. The latter data are from hand fits to the mass spectra, with assigned errors of ± 50% to each point.

is a negligible contribution to the error from uncertainties in the peak positions. (5) Although the absolute level of the cross sections varies with resonance shape, the angular distribution is relatively insensitive to it. We shall see later that the energy dependence is also.

As with elastic scattering there are contributions to N^* cross sections for double scattering in the target, one elastic + one inelastic. In contrast to the case for elastic scattering these are quite small. For the Δ and $N^*(1410)$ the cross sections die at $-t\sim 0.2$ (GeV/c)^2 so the corrections are entirely negligible. For the other N^*'s the correction is maximal at $-t\sim 1$ (GeV/c)^2 where it is 6%. This gives rise to ~1% corrections to A, b, and σ_{N^*} (the integrated values). Because of the shift in missing mass at higher $|t|$ for double scattering vs single scattering, it is questionable how to correct for this effect, considering the fitting procedure. Because of the latter, and since they are sufficiently small, these corrections have not been made.

The final set of differential cross sections for the natural widths listed in Table IV and for $N=2$ is given in Table VI. This table also includes earlier hand fits to the $N^*(2190)$ data at 20.0 and 29.7 GeV/c. The quoted errors include contributions from statistics and from background shape variation only. These data are plotted in Fig. 11.

We remark at this point that (1) all the angular distributions are consistent with a simple exponential dependence, Ae^{bt}, for $|t|<1.0$ (GeV/c)^2, and (2) there is no evidence of a turnover near $|t|\approx 0$ as might occur, for example, in Δ production by π exchange.

E. Exponential Forms and Total Cross Sections

For each N^* the following analyses were performed for each of the nine sets of assumed widths and for $N=1, 2, 3, 10$.

(1) At each energy the differential cross sections at small $|t|$ were fit to the exponential form

$$Ae^{bt}.$$

The t ranges for the Δ and $N^*(1410)$ were $|t|<0.2$

TABLE VI. Differential cross sections for $p+p \to p+N^*$. t values are in $(\mathrm{GeV}/c)^2$ and, except where noted, $d\sigma/dt$ values are in $\mathrm{mb}/(\mathrm{GeV}/c)^2$.

N^* \ P_{inc}	6.2 GeV/c		9.9 GeV/c		15.1 GeV/c		20.0 GeV/c		29.7 GeV/c	
	$-t$	$d\sigma/dt$	$-t$	$d\sigma/dt$	$-t$	$d\sigma/dt$	$-t$	$d\sigma/dt$	$-t$	$d\sigma/dt$
1410			0.011	4.0 ±0.6	0.028	4.3 ±1.4	0.040	2.33 ±0.48	0.070	1.30 ±0.23
			0.020	4.3 ±1.4	0.038	4.2 ±1.0	0.077	1.26 ±0.28	0.104	0.63 ±0.14
			0.028	5.5 ±1.5	0.051	3.0 ±0.7	0.126	0.53 ±0.18	0.146	0.20 ±0.15
			0.048	3.7 ±0.37	0.072	2.42 ±0.54	0.172	0.20 ±0.14		
			0.066	2.9 ±0.29	0.098	2.02 ±0.47	0.223	0.18 ±0.17		
			0.114	1.19 ±0.25	0.127	0.80 ±0.32	0.303	0.07 ±0.12		
			0.198	0.40 ±0.09	0.251	0.091±0.058				
1500			0.018	1.01 ±0.27	0.045	0.77 ±0.27	0.032	0.65 ±0.81	0.070	0.45 ±0.17
			0.058	0.84 ±0.14	0.085	0.62 ±0.15	0.077	0.53 ±0.25	0.104	0.37 ±0.10
			0.114	0.58 ±0.13	0.127	0.75 ±0.14	0.125	0.62 ±0.15	0.145	0.44 ±0.15
			0.197	0.57 ±0.07	0.249	0.28 ±0.07	0.171	0.44 ±0.07	0.193	0.18 ±0.08
			0.270	0.25 ±0.07	0.413	0.151±0.023	0.222	0.29 ±0.06	0.262	0.14 ±0.06
			0.847	0.031±0.007	0.490	0.076±0.017	0.301	0.180 ±0.042	0.375	0.048±0.040
			0.896	0.034±0.006	0.629	0.050±0.015	0.394	0.059 ±0.038	0.489	0.053±0.014
			2.12	1.24 ±0.42 μb	0.747	0.037±0.009	0.497	0.080 ±0.020	0.663	0.020±0.009
			4.57	0.12 ±0.18 μb	2.07	0.72 ±0.38 μb	0.740	0.021 ±0.057	0.766	0.001±0.010
					4.69	0.021±0.028 μb	0.913	0.0118±0.0040		
							1.16	2.5 ±1.2 μb		
							1.41	1.8 ±0.8 μb		
							3.31	0.11 ±0.07 μb		
							3.63	0.03 ±0.03 μb		
1690			0.018	1.63 ±0.20	0.036	1.68 ±0.37	0.040	0.82 ±0.44	0.070	0.91 ±0.17
			0.030	1.19 ±0.41	0.062	1.25 ±0.20	0.077	0.91 ±0.26	0.104	0.87 ±0.12
			0.063	1.53 ±0.14	0.098	1.23 ±0.22	0.125	0.82 ±0.17	0.144	0.60 ±0.16
			0.117	0.88 ±0.11	0.127	0.99 ±0.15	0.169	0.71 ±0.08	0.192	0.48 ±0.09
			0.197	0.79 ±0.08	0.246	0.58 ±0.06	0.220	0.60 ±0.08	0.260	0.34 ±0.09
			0.268	0.45 ±0.07	0.407	0.275±0.030	0.298	0.35 ±0.06	0.372	0.17 ±0.04
			0.826	0.051±0.008	0.482	0.180±0.016	0.389	0.222 ±0.048	0.484	0.110±0.015
			0.874	0.049±0.006	0.618	0.095±0.019	0.490	0.167 ±0.026	0.656	0.046±0.009
			2.06	3.3 ±0.6 μb	0.734	0.061±0.007	0.730	0.035 ±0.006	0.759	0.017±0.011
			4.40	0.16 ±0.23 μb	2.03	0.95 ±0.37 μb	0.900	0.0209±0.0048	1.03	4.4 ±3.5 μb
					4.60	0.051±0.038 μb	1.14	3.3 ±1.4 μb	1.60	0.9 ±0.6 μb
							1.39	2.2 ±1.1 μb	1.98	0.31 ±0.45 μb
							3.26	0.14 ±0.10 μb		
							3.57	0.09 ±0.05 μb		
1236	0.008	3.8 ±1.2	0.012	1.59 ±0.30	0.032	0.93 ±0.54				
	0.050	1.9 ±0.4	0.026	1.6 ±1.1	0.062	0.14 ±0.37				
	0.106	0.95±0.35	0.047	1.35 ±0.35	0.098	0.58 ±0.32				
			0.065	1.06 ±0.17	0.128	0.28 ±0.19				
			0.114	0.52 ±0.15						
			0.200	0.30 ±0.06						
2190							0.072	0.31 ±50%	0.087	0.20 ±50%
							0.103	0.25	0.189	0.143
							0.154	0.18	0.300	0.084
							0.184	0.13	0.554	0.020
							0.217	0.12	0.597	0.017
							0.271	0.080		
							0.353	0.073		
							0.400	0.048		
							0.448	0.029		
							0.660	0.016		
							0.788	0.0066		

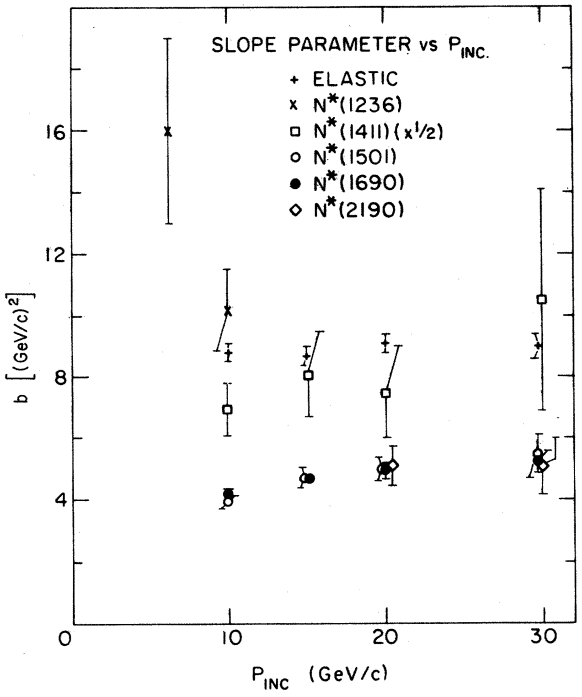

FIG. 12. Logarithmic slopes for pp elastic scattering and N^* production. Note that the slopes for $N^*(1410)$ are plotted with the scale factor $\times\frac{1}{2}$.

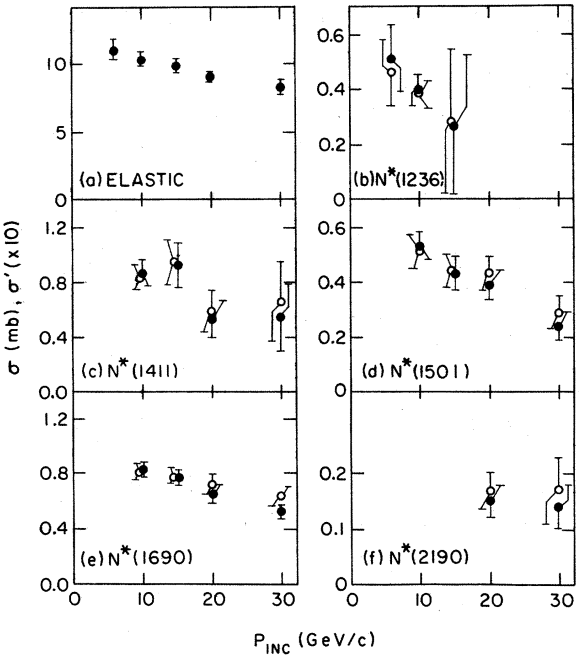

FIG. 13. Total cross sections for pp elastic scattering and N^* production. ● – σ_{el} and σ_{N^*}, ○ – $\sigma' = \sigma_{N^*}/\sigma_{el}$. σ' is plotted with a scale factor of $\times 10$.

$(\mathrm{GeV}/c)^2$, and for the N^*'s at 1500 and 1690 MeV, $|t| < 0.9\ (\mathrm{GeV}/c)^2$.

(2) Total cross sections were evaluated using the relation

$$\sigma_T = 2\int_{t_{\min}}^{\infty} A e^{bt} dt = 2\frac{A}{b} e^{bt_{\min}}, \qquad (6)$$

where the factor 2 comes from the identity of the initial-state protons and the sensitivity of the apparatus to forward recoil protons only.

(3) The total production cross sections, σ_{N^*}, and the ratios $\sigma' = \sigma_{N^*}/\sigma_{el}$ were fit to the phenomenological form

$$\sigma_{N^*} = BP_{\mathrm{inc}}^{-n}, \quad \sigma' = B' P_{\mathrm{inc}}^{-n'}.$$

σ_{el} is the total elastic cross section at the same P_{inc}.

The final values of the quantities A, b, σ_{N^*}, σ', n, and n' are those for the fits with $N = 2$ and with the resonance parameters of Table IV. They are given in Table VII. In addition to statistical errors, also included are separate entries for contributions to the errors from width and shape uncertainties. The errors due to Γ are computed from the errors in the widths in Table IV. The errors due to resonance shape are taken as $\frac{1}{2}$ the spread introduced by N variation. Since the N and Γ contributions are correlated this overestimates their contributions somewhat. Inasmuch as these data have been renormalized by comparison of the elastic data to existing total cross sections, as noted in Sec. IV, we quote a remaining systematic uncertainty in normalization of ±10%. This has not been included in Table VII.

The final values of b and of σ and σ' are plotted vs P_{inc} in Figs. 12 and 13, respectively, along with the corresponding quantities for the elastic scattering data.

For all reactions except Δ production the b parameter is nearly constant with P_{inc}. However, while the elastic slope is $\approx 9\ (\mathrm{GeV}/c)^{-2}$, the $N^*(1410)$ slope is $\approx 15\ (\mathrm{GeV}/c)^{-2}$ and the slopes for N^*'s at 1500, 1690, and 2190 MeV are $\approx 5\ (\mathrm{GeV}/c)^{-2}$. [The value of $\sim 4.0\ (\mathrm{GeV}/c)^{-2}$ for the $N^*(1500)$ and $N^*(1690)$ at 9.9 GeV may be due to including points at $-t \approx 0.9\ (\mathrm{GeV}/c)^2$, where for this low momentum the plot may have ceased to be linear.] Although the Δ slope decreases appreciably from 6.2 to 9.9 GeV/c the quality of these data is such that one cannot consider this to be significant.

Except for the Δ production the plots of σ and σ', Fig. 13, show these quantities to be nearly, if not entirely, independent of P_{inc} for each reaction. The Δ data are sufficiently crude that although cross sections decrease with P_{inc} quantitative estimates of the rate of decrease have large uncertainties.

TABLE VII. Intercepts, slopes, total cross sections and energy dependence for isobar production. Fits are to $d\sigma/dt = Ae^{bt}$; $\sigma_{N^*} = 2A/b$; $\sigma' = \sigma_{N^*}/\sigma_{el}$; $\sigma_{N^*} \propto P^{-n}$; $\sigma' \propto P^{-n'}$. Units are mb/(GeV/c)^2 for A, (GeV/c)$^{-2}$ for b, and mb for σ_{N^*}.

	6.2 GeV/c	9.9 GeV/c	15.1 GeV/c	20.0 GeV/c	29.7 GeV/c
		(a) $N^*(1230)$			
A	4.1 ±0.9	2.0 ±0.4	1.7 ±1.5		
δA_Γ		±0.09	±0.2		
δA_N		±0.20	±0.6		
b	16 ±3	10.2 ±1.3	13 ±12		
δb_Γ		±0.44	±0.8		
δb_N		±0.65	±1.2		
σ_{N^*}	0.51 ±0.05	0.40 ±0.05	0.27 ±0.25		
$(\delta\sigma_{N^*})_\Gamma$		±0.01	±0.02		
$(\delta\sigma_{N^*})_N$		±0.04	±0.07		
σ'	0.046±0.006	0.038±0.005	0.028±0.026		
$\delta\sigma'_\Gamma$		±0.001	±0.02		
$\delta\sigma'_N$		±0.004	±0.07		
		$n = 0.63 \pm 0.32$			
		(b) $N^*(1410)$			
A		6.1 ±0.5	7.5 ±1.4	4.0 ±1.1	5.7 ±2.7
δA_Γ		±1.9	±1.5	±0.9	±1.2
δA_N		±1.9	±3.1	±1.7	±1.8
b		13.9 ±1.7	16.1 ±2.8	15.0 ±3.1	21.0 ±7.2
δb_Γ		±0.4	±0.4	±0.06	±0.3
δb_N		±0.4	±0.5	±0.6	±0.4
σ_{N^*}		0.87 ±0.09	0.93 ±0.16	0.53 ±0.13	0.54 ±0.24
$(\delta\sigma_{N^*})_\Gamma$		±0.21	±0.18	±0.11	±0.13
$(\delta\sigma_{N^*})_N$		±0.29	±0.35	±0.21	±0.16
σ'		0.084±0.009	0.095±0.016	0.059±0.015	0.066±0.029
$\delta\sigma'_\Gamma$		±0.020	±0.019	±0.012	±0.015
$\delta\sigma'_N$		±0.028	±0.036	±0.023	±0.020
		$n = 0.50 \pm 0.30$	$n' = 0.28 \pm 0.29$		
		$\delta n_\Gamma =$ ±0.05	$\delta n'_\Gamma =$ ±0.04		
		$\delta n_N =$ ±0.05	$\delta n'_N =$ ±0.08		
		(c) $N^*(1500)$			
A		1.03 ±0.09	1.02 ±0.15	0.94 ±0.14	0.65 ±0.15
δA_Γ		±0.09	±0.21	±0.17	±0.10
δA_N		±0.35	±0.28	±0.31	±0.18
b		3.93 ±0.20	4.72 ±0.32	4.99 ±0.35	5.44 ±0.68
δb_Γ		±0.14	±0.08	±0.08	±0.12
δb_N		±0.08	±0.21	±0.11	±0.08
σ_{N^*}		0.53 ±0.05	0.43 ±0.06	0.39 ±0.05	0.24 ±0.05
$(\delta\sigma_{N^*})_\Gamma$		±0.10	±0.10	±0.06	±0.04
$(\delta\sigma_{N^*})_N$		±0.18	±0.12	±0.11	±0.06
σ'		0.051±0.006	0.044±0.006	0.043±0.006	0.029±0.006
$\delta\sigma'_\Gamma$		±0.010	±0.010	±0.007	±0.005
$\delta\sigma'_N$		±0.017	±0.012	±0.012	±0.007
		$n = 0.56 \pm 0.06$	$n' = 0.38 \pm 0.09$		
		$\delta n_\Gamma =$ ±0.04	$\delta n'_\Gamma =$ ±0.04		
		$\delta n_N =$ ±0.09	$\delta n'_N =$ ±0.08		

TABLE VII *(Continued)*

	6.2 GeV/c	9.9 GeV/c	15.1 GeV/c	20.0 GeV/c	29.7 GeV/c
			(d) $N^*(1690)$		
A		1.73 ±0.11	1.81 ±0.15	1.60 ±0.17	1.35 ±0.16
δA_Γ		±0.22	±0.22	±0.21	±0.14
δA_N		±0.63	±0.61	±0.52	±0.43
b		4.21 ±0.14	4.70 ±0.20	4.95 ±0.25	5.25 ±0.32
δb_Γ		±0.05	±0.04	±0.03	±0.06
δb_N		±0.02	±0.02	±0.04	±0.07
σ_{N^*}		0.83 ±0.05	0.77 ±0.05	0.65 ±0.06	0.52 ±0.06
$(\delta\sigma_{N^*})_\Gamma$		±0.10	±0.09	±0.07	±0.04
$(\delta\sigma_{N^*})_N$		±0.28	±0.26	±0.20	±0.16
σ'		0.081±0.006	0.078±0.006	0.072±0.007	0.063±0.007
$\delta\sigma'_\Gamma$		±0.010	±0.009	±0.008	±0.006
$\delta\sigma'_N$		±0.027	±0.027	±0.022	±0.020
		n =0.34 ±0.06		n'= 0.18 ±0.03	
		δn_Γ= ±0.03		$\delta n'_\Gamma$ = ±0.03	
		δn_Γ= ±0.04		$\delta n'_N$ = ±0.04	
			(e) $N^*(2190)$		
A				0.39 ±0.08	0.35 ±0.12
b				5.1 ±0.6	5.1 ±0.9
σ				0.15 ±0.03	0.14 ±0.04
σ'				0.017±0.003	0.017±0.006
		n =0.17±0.84		n' =0.0±0.74	

VI. DISCUSSION

A. Identification of the Observed N^*'s

We have deferred until now discussion of what precisely constitute the so-called N^*'s observed in this experiment. Only the Δ resonance is uniquely defined in phase-shift analyses. The $N^*(1410)$ is most usually identified as either the $P_{11}(1470)$ π-p resonance, a kinematic effect in the spirit of Drell and Hiida,[25] or as a combination of the two. Among the well-established resonances in phase-shift analyses (see Table IV) there are two possible candidates for the $N^*(1500)$, five for the $N^*(1690)$, and one for the $N^*(2190)$. Although much work has been done on this problem using both counter and bubble-chamber techniques, it has still not been clearly resolved.

1. *The N^*'s at 1500, 1690, and 2190 MeV*

We shall exclude the Δ from further discussion here and speak first about the N^*'s at 1500, 1690, and 2190 MeV. These N^*'s all have integrated cross sections which are nearly independent of P_{inc}. They all have candidates from phase-shift analyses with $I=\frac{1}{2}$ and also with spin and parity, $J=l+\frac{1}{2}$ and $P=(-1)^l$, consistent with production by natural spin-parity exchange. These are factors which are consistent with production through diffraction dissociation,[26] or in other words through Pomeranchuk-trajectory exchange. Thus it is suggested that dominantly their identification is as follows: $N^*(1500)\equiv D_{13}(1520)$, $N^*(1690)\equiv F_{15}(1688)$, and $N^*(2190)\equiv G_{17}(2190)$.

Although the following argument is speculative there is additional evidence which supports the identification as unique states rather than as composite bumps: (1) In this experiment, for a wide range of values of s and t the positions and widths of these bumps are constant. Furthermore, from Table IV there is excellent agreement with the results of other missing-mass experiments on p-p, π^--p, and e-p scattering. While the errors on the widths in these experiments are fairly large the positions have been determined in most cases to a few MeV. (2) As is seen particularly well for the $N^*(1690)$, in this experiment the production cross sections for each N^* follow a simple exponential dependence on t at each P_{inc} [$-t<1$ (GeV/c)^2], and are essentially independent of P_{inc}. Conversely, states which cannot be produced through Pomeranchuk exchange would be expected to have cross sections which decrease rapidly with energy. These features suggest the dominance in production of a unique state rather than the competition of two or more, and furthermore that the identification above is probably correct.

It has been argued by Morrison[27] that in fact the $N\pi$ and $N\pi\pi$ decays of the $N^*(1690)$ peak at significantly different masses, particularly in π-p and K-p scattering, and there is some suggestion in bubble-chamber data that their widths are also different. He assigns the positions 1690 and 1730

MeV to the $N\pi$ and $N\pi\pi$ systems, respectively, and proceeds to suggest that the two systems are produced by different mechanisms. We observe, however, from Table IV, that there is a wide range of possible positions for the $N\pi\pi$ system, and therefore, no such separation is required by the data. In any case small differences in position are possible for different decay channels of the same resonance.[15] It should be kept in mind that the bubble-chamber spectra are typically given integrated over t, whereas the counter spectra are at discreet t values. In the present experiment for example the resonance parameters for the $N^*(1690)$ were determined for $-t > 0.2$ (GeV/c)^2. If this suggestion of two contributing processes should be confirmed, the possibility remains that one of them is significant for $-t < 0.2$ (GeV/c)^2 only.

2. *The N*(1410)*

There remains the question of the $N^*(1410)$, first observed in a missing-mass experiment by Bellettini *et al.*[20] As mentioned above, it is possible to associate this N^* with the $P_{11}(1470)$. Although the resonance is broad, the distinction between 1411 and 1470 MeV makes this assignment somewhat questionable. Also, decay angular distribution studies in production experiments[28] do not clearly confirm the assignment $J = \frac{1}{2}$. As can be seen from Table IV most bubble-chamber results find the position to be significantly higher than 1411. However, again typically, these spectra are integrated over all t. In this case there will be a significant shift in the signal toward higher mass due to the inclusion of the $N^*(1500)$ signal. Again, the possibility exists that the peak positions of the $N\pi$ and $N\pi\pi$ signals are significantly different.[27] It should be kept in mind that our detailed studies are for $P_{\text{inc}} \geq 9.9$ GeV/c and that data at lower momenta may lead to significantly different conclusions.

The $N^*(1410)$ is seen primarily in production experiments with $\Delta Q = 0$ and in p, $\bar{p}$, π, and K beams.[29] There is also some evidence[30] for charge-exchange production of the N^{*0}. However, it is striking that there is no significant $N^*(1410)$ signal in e-p scattering[18,31] despite the prominence in these data of other $I = \frac{1}{2}$ N^*'s. It is apparent that this enhancement is uniquely different from the nucleon and others of its excited states.

One possible solution to this question resides in the quark model of the baryons,[32] wherein the $P_{11}(1470)$ is taken to be due to the radial excitation of one of the quarks in the nucleon, while the other $I = \frac{1}{2}$ N^*'s are due to orbital excitation. Thus it may be that Coulomb excitation of this state may be inhibited vis-à-vis hadron or Pomeranchuk exchange.

There have also been numerous calculations of the Drell-Hiida-type mechanism, with or without final-state interactions, typified more recently by the work of Berger.[33] In a "semi-quantitative" fashion these calculations are able to reproduce this enhancement, and although it may not give a complete description of the production process this mechanism must play an important role. Thus the possibility exists that the enhancement called the $N^*(1410)$ is not a proper particle but rather a "kinematical" effect, or dominantly so.

B. s and t Dependence of N^* Production

1. Δ *Production*

Both single and double Δ production in nucleon-nucleon collisions appear to be dominated by π exchange. Fits of integrated cross sections to P^{-n} give the n values 2.2 ± 0.16 for $pp \to n\Delta^{++}$ (see Ref. 34), 2.0 ± 0.3 for $pp \to p\Delta^{+}$ (see Ref. 21), and 2.5 ± 0.3 for a combination of $pp \to \Delta^{++}\Delta^{0}$, $pn \to \Delta^{++}\Delta^{-}$, and $\bar{p}p \to \Delta^{++}\bar{\Delta}^{--}$ (see Ref. 35), all in good agreement with the expected value of 2 for π exchange. The value $n = 0.63 \pm 0.32$ for the present data most probably reflects the considerable difficulty of extracting this small cross section from a large and rapidly varying total signal. The cross sections at 6.2 and 9.9 GeV/c are in fact in good agreement and the t slopes in reasonable agreement with those of other experiments.[21,36] The recent measurement[29] of $\bar{p}p \to \bar{p}\Delta^{+}$ at 8 GeV/c yields the t slope 9.1 ± 1.2 (GeV/c)$^{-2}$ in reasonable agreement with the values quoted above. Comparing with the extrapolated cross section for this reaction at 9.9 GeV/c, we find

$$\frac{\sigma_T(pp \to p\Delta^{+})}{\sigma_T(\bar{p}p \to \bar{p}\Delta^{+})} = 1.73 \pm 0.28,$$

where the error is statistical only. Considering the additional uncertainty in normalization of $\pm 35\%$ for each reaction because of the fitting procedure this ratio is in fair agreement with the value 1.0 expected for pure π exchange.

It has been shown assuming duality that the imaginary part of the Δ production amplitudes must vanish.[37] This has led to the suggestion[38] that these reactions must be dominated by π exchange which is expected to give rise to dominantly real amplitudes. The result of our comparison does not disagree with this hypothesis although the errors do not allow for a stringent test.

2. $N^*_{1/2}$ *Production*

As has been discussed above, an important objective of the extensive computer studies of the resonance cross sections was to demonstrate that the t slopes and energy-dependence parameters, b and n, are well determined in this experiment,

i.e., that they are relatively insensitive to a broad range of resonance and background shapes. This is well borne out by the data shown in Table VII. In all cases the uncertainties in b and n due to width and shape uncertainties are comparable to or smaller than the "statistical errors" (the latter include contributions from background variation as discussed in Sec. V). On the other hand, the corresponding uncertainties in absolute normalization are typically ±35%.

From 15.1 to 29.7 GeV/c and for $-t<0.9$ (GeV/c)^2 the t slopes for the N^*'s at 1500, 1690, and 2190 MeV are all ≈5 (GeV/c)$^{-2}$. At 9.9 GeV/c the slopes for the $N^*(1500)$ and $N^*(1690)$ are ~4 (GeV/c)$^{-2}$, however, fitting to the smaller t range, $-t<0.3$ (GeV/c)^2, we find slopes of 4.2 ± 0.5 and 4.5 ± 0.3 (GeV/c)$^{-2}$. The slopes for the $N^*(1500)$ and $N^*(1690)$ are consistent with the results of Blair *et al.*[29] at lower momenta, and considering the normalization uncertainties the cross sections are also.

For the $N^*(1690)$ we have used the above slope for 9.9 GeV/c and the slopes for the higher momenta from Table VII to evaluate the slope of the effective Regge trajectory at $t=0$. We find

$$\alpha_{1690}'(0)=0.38\pm0.17.$$

Since the slopes are insensitive to resonance-shape variation this value is considered to be reliable. A similar behavior is seen for the $N^*(1500)$ but with larger errors. We note that while this "shrinkage" is reasonably compatible with the very small shrinkage seen in the slopes for our elastic scattering data, it is also in good agreement with the value $\alpha'=0.47\pm0.09$ obtained at Serpukhov[39] from elastic scattering in the range $0.008<-t<0.12$ (GeV/c)^2. If these cross sections are dominated by Pomeranchuk exchange, these data tend to support a trajectory with a nonzero slope.

As was first demonstrated in Ref. 2 the $N^*(1500)$ and $N^*(1690)$ cross sections vary more slowly with t for $-t>1$ (GeV/c)^2. Although the discontinuities in the t dependence are not as pronounced as for elastic scattering, qualitatively the behavior is quite similar both in t and $P_{\rm inc}$ dependence. Roughly speaking both types of reactions show t slopes consistent with ~1.6 (GeV/c)$^{-2}$ and decrease rapidly with $\sim P_{\rm inc}$. (The elastic cross sections decrease in this region like $P_{\rm inc}^{-2}$, however, the N^* cross sections are too crudely measured to assign a reliable $P_{\rm inc}$ dependence.) This behavior has been studied in detail more recently by Allaby *et al.*,[40] who reach similar conclusions, and, where comparable, our results are in good agreement. A similar behavior was also observed by Ankenbrandt, *et al.*[19] at lower momenta.

Several authors[41] have suggested that this structure in the t dependence at high $|t|$ can be explained by multiple hadron-hadron scattering, which gives rise to ever decreasing slopes as $|t|$ increases. While they are able to give qualitative description of the data, no quantitative fit has so far been made. Also the similarity in behavior between the elastic scattering and the isobar-production data is consistent with a statistical type of model[42] for two-body scattering at high $|t|$ wherein the behavior of the cross sections is similar regardless of the final state.

The t slopes for the $N^*(1410)$ show no clear evidence of energy dependence though they are also compatible with the shrinkage found for the $N^*(1690)$. They average to ≈15 (GeV/c)$^{-2}$ for all the data from 9.9 to 29.7 GeV/c.

The essential lack of energy dependence of the $N_{1/2}^*$ production cross sections is most striking. For every case, it appears that there is a small residual energy dependence beyond the amount $n=0.20\pm0.05$ seen for elastic scattering. For example, for the $N^*(1690)$ $n'=0.18\pm0.03$ using the full fit to the 9.9-GeV/c data and $n'=0.06\pm0.04$ using the restricted fit to these data discussed above. These values are considerably smaller than those found for any other two-body processes for which there is necessarily internal-quantum-number exchange. The near constancy of these cross sections is generally attributed to the diffraction-dissociation process.[26] We point out that this approach need not regenerate N^*'s with constant cross sections if the constituent diffractive processes are energy-dependent. However, inasmuch as the p-p total cross sections are nearly constant in this energy range the diffraction scattering is also. This being the case N^* regeneration is expected to hold up with energy.

There has been no definitive explanation of the t slopes of ~15 and ~5 (GeV/c)$^{-2}$ found in the $N_{1/2}^*$ data. Several authors[32,41] have suggested variations on the hadron-hadron multiple-scattering mechanism to explain this effect. Thus $N^*(1410)$ production derives from single scattering and $N^*(1690)$ production from double scattering.

3. *Factorization in $N_{1/2}^*$ Production*

In addition to p-p scattering, N^* production has been observed in e-p scattering[18,31] and, in the sequel to the present experiment, in π^--p, K^--p, and $\bar{p}$-p scattering.[17,29] Since the $N^*(1690)$ data are the most reliably determined we shall discuss only these and the elastic scattering in connection with factorization. It is instructive to look first at the t distributions for the individual processes, since it is apparent from these that N^* production and separately elastic scattering are somewhat parti-

cle-dependent. p-p and $\bar{p}$-p N^* production and elastic scattering data are reasonably well fit by simple exponentials in t for $-t<0.6$ $(\mathrm{GeV}/c)^2$, whereas the distributions for π^--p and K^--p scattering show definite curvature in the small-$|t|$ region. Thus these processes are only approximately particle-independent at these energies and one should therefore expect only approximate factorization to hold.

References 17 and 29 give plots of $(d\sigma_{N^*}/dt)/(d\sigma_{\mathrm{el}}/dt)$ vs t for $N^*(1690)$ produced in p-p, π^--p, K^--p, $\bar{p}$-p, and e-p scattering. These show that for the hadron scattering there is excellent agreement with factorization in the region $-t<0.3$ $(\mathrm{GeV}/c)^2$, and that the electron data while they show a similar behavior lie a factor of 2 higher. The errors inherent in the fitting procedure can easily account for the differences in normalization in the hadron scattering. However, the differences between electron and hadron scattering are probably too large to be accounted for by this means alone. All in all this evidence for factorization in hadron-hadron scattering is important additional corroboration of the dominance of Pomeranchuk trajectory exchange in these processes.

On this basis one is now led to predictions for double $N^*_{1/2}$ production. One expects that

$$\sigma_D=\sigma_S{}^2/\sigma_{\mathrm{el}},$$

where $\sigma_D, 2\sigma_S$, and σ_{el} are the cross sections for $pp\to N^{*+}_{1/2}N^{*+}_{1/2}$, $pp\to pN^{*+}_{1/2}$, and $pp\to pp$, respectively. Using the data of Table VII, we predict

$$\sigma_D\approx 0.06 \text{ mb at } 29.7 \text{ GeV}/c.$$

All combinations of double $N^*_{1/2}$ production and all decay modes are included in this prediction. So far attempts to observe these processes[43] have given no clear evidence of them, however the sensitivity has been insufficient for this cross-section level.

C. On the Nonresonant Background in the Mass Spectra

We have not attempted to discuss the background in the missing-mass spectra, as the data have already been published,[4] and no new work has been done for this paper. However, we note that recently there has been a great deal of interest in inclusive processes stimulated in part by the fundamental work of Mueller.[44] In particular, the present data have recently[45] been used by Edelstein, Rittenberg, and Rubinstein to study the validity of duality in the triple-Regge limit. They find that the data are consistent with the background being dual to the Pomeranchuk trajectory as postulated by Harari[46] and Freund,[47] and through its t dependence, are able to study its production mechanism as well. Thus, at small t, while the N^*'s are produced by Pomeranchuk exchange the background production is dominated by normal trajectory exchange. The latter accounts for the decreasing with energy of the background already discussed. More work of a quantitative nature must be done, but it is to be hoped that an important dividend of this approach will be a better understanding of how to fit missing-mass spectra.

ACKNOWLEDGMENTS

It is a great pleasure to thank the many people at the Brookhaven AGS who helped make this experiment possible. We are indebted to the BNL Instrumentation Division and in particular to J. Fischer for building the wire chambers and W. Higinbotham whose group built the read-out electronics. We also thank the Carnegie-Mellon University engineering staff, in particular J. Thompson, for his work on the Čerenkov counter. S. Heller was an important part of the on-line software team. Our able technicians were R. Rothe, E. Bihn, and J. Smith. We are particularly indebted to D. Thomas who carried through much of the computer fitting job.

One of us (R.M.E.) wishes to express his appreciation to the Weizmann Institute of Science for its generous hospitality during a sabbatical year, without which this paper would not have been written.

---

*Work supported by the U. S. Atomic Energy Commission.

†Weizmann Institute Fellow during the Academic Year 1970–1971.

‡Present address: National Accelerator Laboratory, Batavia, Ill. 60510.

§Present address: T. J. Watson Laboratory, Yorktown Heights, N. Y.

¶Present address: University of Birmingham, Birmingham, England.

**Present address: Leech Farm V. A. Hospital, Pittsburgh, Pa. 15206.

††Present address: Institute for Nuclear Study, University of Tokyo, Tanashi, Tokyo, Japan.

‡‡Present address: 146/32 Bar Yochai, Katamon 9, Jerusalem, Israel.

[1]Discussion of what constitute the bumps in the missing-mass spectra is deferred to Sec. VI. For the most part

they will be called N^*'s in the interest of brevity.

[2]E. W. Anderson, E. J. Bleser, G. B. Collins, T. Fujii, J. Menes, F. Turkot, R. A. Carrigan, Jr., R. M. Edelstein, N. C. Hien, T. J. McMahon, and I. Nadelhaft, Phys. Rev. Letters 16, 855 (1966).

[3]R. A. Carrigan, Jr., R. M.Edelstein, N. C. Hien, T. J. McMahon, I. Nadelhaft, E. W. Anderson, E. J. Bleser, G. B. Collins, T. Fujii, J. Menes, and F. Turkot, Phys. Rev. Letters, 24, 683 (1970).

[4]E. W. Anderson, E. J. Bleser, G. B. Collins, T. Fujii, J. Menes, F. Turkot, R. A. Carrigan, Jr., R. M. Edelstein, N. C. Hien, T. J. McMahon, and I. Nadelhaft, Phys. Rev. Letters 19, 198 (1967).

[5]E. J. Bleser, G.B. Collins, J. Fischer, T. Fujii, S. Heller, W. Higinbotham, J. Menes, H. Pate, F. Turkot, and N. C. Hien, Nucl. Instr. Methods 44, 1 (1966).

[6]The spectra in Fig. 5 are, properly speaking, plots of $d^2\sigma/dW\,d\Omega_{\rm lab}$ scaled by the factor $d\Omega_{\rm lab}/dt$ appropriate to $W=1500$ MeV. The t values given are also for fixed angle and $W=1500$ MeV. The distinction between this and converting to t before binning is negligible for the purpose at hand, but the reader is well advised to consider this point before extracting data from these plots.

[7]For Figs. 5(c) and 5(d) in order to present all data at the same fixed t values, the spectrum for $P_{\rm inc}=29.7$ GeV/c and $-t=0.044$ (GeV/c)^2 was extrapolated from $-t=0.057$ (GeV/c)^2, and the 15.1 GeV/c spectrum at 0.88 (GeV/c)^2 was extrapolated from $-t=0.73$ (GeV/c)^2, both using a local exponential t dependence. The spectra are presented for illustrative purposes only, they were not used for cross-section evaluation.

[8]K. J. Foley, R. S. Jones, S. J. Lindenbaum, W. A. Love, S. Ozaki, E. D. Platner, C.A. Quarles, and E. H. Willen, Phys. Rev. Letters 19, 857 (1967).

[9]G. Belletini, G. Cocconi, A. N. Diddens, E. Lillethun, J. Pahl, J. P. Scanlon, J. Walters, A. M. Wetherell, and P. Zanella, Phys. Letters 14, 164 (1965); 19, 705 (1966).

[10]The renormalization factor for 29.7 GeV/c for the straightforward fit to the quadratic exponential is 1.28. However, recently there has been speculation (see Ref. 11) that at high energy there may be a larger slope parameter b for $-t<0.2$ (GeV/c)^2 than for higher $|t|$. This would provide a ready explanation for the apparently large renormalization factor. While such a change in b is consistent with our small-$|t|$ data there is insufficient evidence for establishing the effect. On the other hand, we are unable to find any reason for such a large error in absolute normalization. We therefore assign the renormalization factor 1.17 ± 0.11 which is intermediate between 1.28 and 1.06 (the latter is the average of the factors for 6.2, 9.9, 15.1, and 20.0 GeV/c. Because of this uncertainty there is a corresponding range of $\pm6\%$ in the quoted total elastic cross section.

[11]R. A. Carrigan, Jr., Phys. Rev. Letters 24, 168 (1970).

[12]K. J. Foley, R. S. Gilmore, S. J. Lindenbaum, W. A. Love, S. Ozaki, E. H. Willen, R. Yamada, and L. C. L. Yuan, Phys. Rev. Letters 15, 45 (1965); D. Harting, P. Blackall, B. Elsner, A. C. Helmholz, W. E. Middelkoop, B. Powell, B. Zacharov, P. Zanella, P. Dalpiaz, M. N. Focacci, S. Focardi, G. Giacomelli, L. Monari, J. A. Beaney, R. A. Donald, P. Mason, L. W. Jones, and D. O. Caldwell, Nuovo Cimento 38, 60 (1965).

[13]J. V. Allaby, A. N. Diddens, R.W. Dobinson, A. Klovning, J. Litt, L. S. Rochester, K. Schlüpmann, A. M. Wetherell, U. Amaldi, R. Biancastelli, C. Bosio, and G. Matthiae, Phys. Letters 34B, 431 (1971); J. V. Allaby, F. Binon, A. N. Diddens, P. Duteil, A. Klovning, R. Meunier, J. P. Peigneux, E. J. Sacharidis, K. Schlüpmann, M. Spighel, J. P. Stroot, A. M. Thorndike, and A. M. Wetherell, *ibid.* 28B, 67 (1968).

[14]Although properly speaking $W_{\rm th}=1.073$ GeV, it was arbitrarily set to 1.05 GeV to account for smearing due to finite resolution.

[15]J. D. Jackson, Nuovo Cimento 34, 1644 (1964).

[16]Fits in this t region with the $N^*(1500)$ included gave cross sections for it which were consistent with zero and as often negative as positive. The procedure adopted was, therefore, less subject to error.

[17]E. W. Anderson, E. J. Bleser, H. R. Blieden, G. B. Collins, D. Garelick, J. Menes, F. Turkot, D. Birnbaum, R. M. Edelstein, N. C. Hien, T. J. McMahon, J. F. Mucci, and J. S. Russ, Phys. Rev. Letters 25, 699 (1970).

[18]M. Breidenbach, MIT Report No. 2098-635, 1970 (unpublished).

[19]C. M. Ankenbrandt, A. R. Clark, Bruce Cork, T. Elioff, L. T. Kerth, and W. A. Wentzel, Phys. Rev. 170, 1223 (1968).

[20]G. Belletini, G. Cocconi, A. N. Diddens, E. Lillethun, J. P. Scanlon, A. M. Shapiro, and A. M. Wetherell, Phys. Letters 18, 167 (1965).

[21]I. M. Blair, A. E. Taylor, W. S. Chapman, P. I. P. Kalmus, J. Litt, M. C. Miller, H. J. Sherman, A. Astbury, D. B. Scott, and T. C. Walker, Nuovo Cimento 63A, 529 (1969).

[22]A. A. Carter, J. R. Williams, D. V. Bugg, P. J. Bussey, and D. R. Dance, unpublished report, presented at the Fifteenth International Conference on High-Energy Physics, Kiev, U.S.S.R., 1970. See also Ref. 23.

[23]These data are taken from Table IV of a paper by R. J. Plano, in *Proceedings of the Fifteenth International Conference on High Energy Physics, Kiev, U.S.S.R., 1970* (Atomizdat, Moscow, 1971).

[24]Particle Data Group (David J. Herndon, Angela Barbaro-Galtieri, and Arthur Rosenfeld), LRL Report No. UCRL 20030 πN, 1970 (unpublished).

[25]S. D. Drell and K. Hiida, Phys. Rev. Letters 7, 199 (1961).

[26]M. L. Good and W. D. Walker, Phys. Rev. 120, 1857 (1960).

[27]D. R. O. Morrison, in *Proceedings of the Fifteenth International Conference on High Energy Physics, Kiev, U.S.S.R., 1970* (Atomizdat, Moscow, 1971).

[28]See, for example, J. I. Rhode, R. A. Leacock, W. J. Kernan, R. A. Jesperson, and T. L. Schalk, Phys. Rev. 187, 1844 (1969).

[29]E. W. Anderson, E. J. Bleser, H. R. Blieden, G. B. Collins, D. Garelick, J. Menes, F. Turkot, D. Birnbaum, R. M. Edelstein, N. C. Hien, T. J. McMahon, J. F. Mucci, and J. S. Russ (unpublished).

[30]R. B. Bell, D. J. Crennell, P. V. C. Hough, U. Karshon, K. W. Lai, J. M. Scarr, T. G. Schumann, I. O. Skillicorn, R. C. Strand, A. H. Bachman, P. Baumel, R. M. Lea, and A. Montwill, Phys. Rev. Letters 20, 164 (1968).

[31]E. D. Bloom, R. L. Cottrell, D. H. Coward, H. De Staebler, Jr., J. Drees, G. Miller, L. W. Mo,

R. E. Taylor, J. I. Friedman, G.C. Hartmann, and H. W. Kendall, SLAC Report No. SLAC-PUB-653, 1969 (unpublished).

[32]A. W. Hendry and J. S. Trefil, Phys. Rev. 184, 1680 (1969).

[33]E. L. Berger, Phys. Rev. 179, 1567 (1969).

[34]Particle Data Group (O. Benary, L. R. Price, and G. Alexander), LRL Report No. UCRL 20000 *NN*, 1970 (unpublished).

[35]A. Shapira, G. Yekutieli, D. Yaffe, S. Toaff, E. E. Ronat, L. Lyons, U. Karshon, B. Haber, and Y. Eisenberg, Nucl. Phys. B23, 583 (1970).

[36]H. C. Dehne, J. Diaz, K. Strömer, A. Schmitt, W. P. Swanson, I. Borecka, G. Knies, and G. Wolf, Nuovo Cimento 53A, 232 (1968).

[37]J. L. Rosner, C. Rebbi, and R. Slansky, Phys. Rev. 188, 2367 (1969).

[38]M. Kugler, Phys. Letters 32B, 107 (1970).

[39]G. G. Beznogikh, A. Buyak, K. I. Iovchev, L. F. Kirillova, P. K. Markov, B. A. Morozov, V. A. Nikitin, P. V. Nomokonov, M. G. Shafranova, V. A. Sviridov, Truong Bien, V. I. Zayachki, N. K. Zhidkov, L. S. Zolin, S. B. Nurushev, and V. L. Solovianov, Phys. Letters 30B, 274 (1969).

[40]U. Amaldi, R. Biancastelli, C. Bosio, G. Matthiae, J. V. Allaby, A. N. Diddens, R. W. Dobinson, A. Klovning, J. Litt, L. S. Rochester, K. Schlüpmann, and A. M. Wetherell, Phys. Letters 34B, 435 (1971); J. V. Allaby, F. Binon, A. N. Diddens, P. Duteil, A. Klovning, R. Meunier, J. P. Peigneux, E. J. Sacharidis, K. Schlüpmann, M. Spighel, J. P. Stroot, A. M. Thorndike, and A. M. Wetherell, *ibid.* 28B, 229 (1968).

[41]S. Frautschi and B. Margolis, Nuovo Cimento 56A, 1155 (1968); 57A, 427 (1968); C. B. Chiu and J. Finkelstein, *ibid.* 57A, 649 (1968); 59A, 92 (1969).

[42]J. Benecke, T. T. Chou, C. N. Yang, and E. Yen, Phys. Rev. 188, 2159 (1969); R. Hagedorn, Nuovo Cimento 35, 216 (1965); T. T. Wu and C. N. Yang, Phys. Rev. 137, B708 (1965).

[43]I. R. Kenyon, Nucl. Phys. B13, 255 (1969).

[44]A. H. Mueller, Phys. Rev. D 2, 2963 (1970).

[45]R. M. Edelstein, V. Rittenberg, and H. R. Rubinstein, Phys. Letters 35B, 408 (1971).

[46]H. Harari, Phys. Rev. Letters 20, 1395 (1968).

[47]P. G. O. Freund, Phys. Rev. Letters 20, 235 (1968).